Alma Mater Studiorum – University of Bologna

School of Science

Department of Physics and Astronomy

Master Degree Programme in Astrophysics and Cosmology

Assessing the chemical DNA of Liller1: a spectroscopic insight of the Galactic Bulge formation

Graduation Thesis

Presented by:

Alessia Bartolomei

Supervisor: **Chiar.mo Prof. F.R. Ferraro**

Co-supervisor: **Lanfranco Chiappino**

Academic Year 2023/2024

Graduation date 29/10/2024 - Session III

Contents

Abstract

In agreement with the observation of chain and clumpy galaxies in the distant Universe (out to redshift z∼6; e.g., Elmegreen et al. 2009; Genzel et al. 2011; Tacchella et al. 2015), bulges of spiral galaxies form through multiple mergers of massive clumps of gas and stars generated by disk instability and fragmentation (e.g., Immeli et al. 2004; Elmegreen et al. 2008; Bournaud & Elmegreen 2009; Bournaud 2016). While the majority of these clumps are predicted to dissolve and form the bulge, a few of them may have survived and now broadly appear as globular clusters (Bournaud 2016). At odds with the latter, however, these "Bulge Fossil Fragments" (BFFs) should host multi-iron and multi-age sub-populations, with the same "chemical DNA" of the bulge. Indeed, a few specific abundance patterns (for instance, [α/Fe] versus [Fe/H]) univocally trace the timescales and efficiency of the enrichment process of the interstellar medium from which stars formed, thus providing authentic “chemical DNA tests” of their origin.

Hence, the study of the Galactic Bulge, in particular the chemical tagging of its globular cluster population, is of fundamental importance to probe the early history of the Milky Way assembling. Indeed, this is the only spheroid where individual stars can be observed and where an in-depth study of the kinematic, photometric and chemical properties of the stellar populations can be conducted.

In this work I present the chemical screening of a sample of 10 stars in the GC-like stellar system Liller 1, one of the candidate BFFs discovered so far (Ferraro et al., 2021a). The data have been acquired with the NIR echelle spectrograph CRIRES+ at the ESO-Very Large Telescope (VLT) through the ongoing Large Programme P110.24A4 (255 hours, PI: Ferraro). This project is part of the Bulge Cluster Origin (BulCO) survey, which aims at performing the same chemical analysis on a large sample of representative Bulge stellar systems, searching in each of them a fragment of the early history of our galaxy. The high resolution of the CRIRES+ spectra (R=50,000) makes them ideal for the safe identification and measurement of a multitude of atomic and molecular spectral lines, including those of the most powerful chemical DNA indicators, such as iron, α-elements and iron-peak elements as Scandium and Vanadium.

The chemical analysis of the spectra (obtained in the H and K-band) performed with the well-tested spectral synthesis technique allowed the measure of the abundances of key elements, like iron, calcium, silicon and magnesium. Despite the limited sample size, this study has confirmed the presence of multiple iron populations within Liller 1, thus solidly constraining its nature spectroscopically and advancing our understanding of this intriguing object.

This thesis is organized as follows:
The initial chapter (Chapter 1) presents the scientific context. The subsequent chapter (Chapter 2) delineates the characteristics of the database, while Chapter 3 outlines the techniques employed for the spectral and chemical analysis. Finally, Chapter 4 presents the final results and displays conclusions and future perspectives.

Chapter 1

Introduction

1.1 Bulge formation history

The Galactic Bulge is one of the fundamental components of the Milky Way (MW), containing about one quarter of the total stellar mass ($2{\cdot}10^{10} M_{\odot}$; Valenti et al. 2016) and representing the first massive component of the Galaxy to have collapsed into stars (12-13 Gyrs ago). Unfortunately, its formation history remains an extremely debated subject.

The Λ-Cold Dark Matter (ΛCDM) cosmological model (Davis et al. 1985) predicts that cosmic structures follow a bottom-up formation scenario through hierarchical merging processes. Basically, smaller masses, such as clumps of stars and gas, collapse first, and then they assemble through collisions and mergers into galaxies, clusters of galaxies, and superclusters. This model successfully explains the existence and the observed properties of massive galaxy and galaxy clusters.

The unprecedented exploration of our galaxy performed by the Gaia mission has actually identified several kinematic structures (as Gaia-Enceladus, Helmi stream, Sequoia, etc.) associated to past accretion events suffered by the MW halo (Helmi 2020). This stunning discovery suggests that the majority of the surveyed globular clusters (GCs) seem to be associated to known merging events or have an unclear origin, and only $\sim 40\%$ of them has an in-situ formation (Massari et al. 2019).

It is reasonable to expect that also the Galactic bulge experienced past accretion events, which left clear signatures imprinted in its old stellar populations. Unluckily, due to its high density and reddening conditions, no conclusive observational results have been obtained so far and several mechanisms have been proposed to explain the Galactic bulge formation.

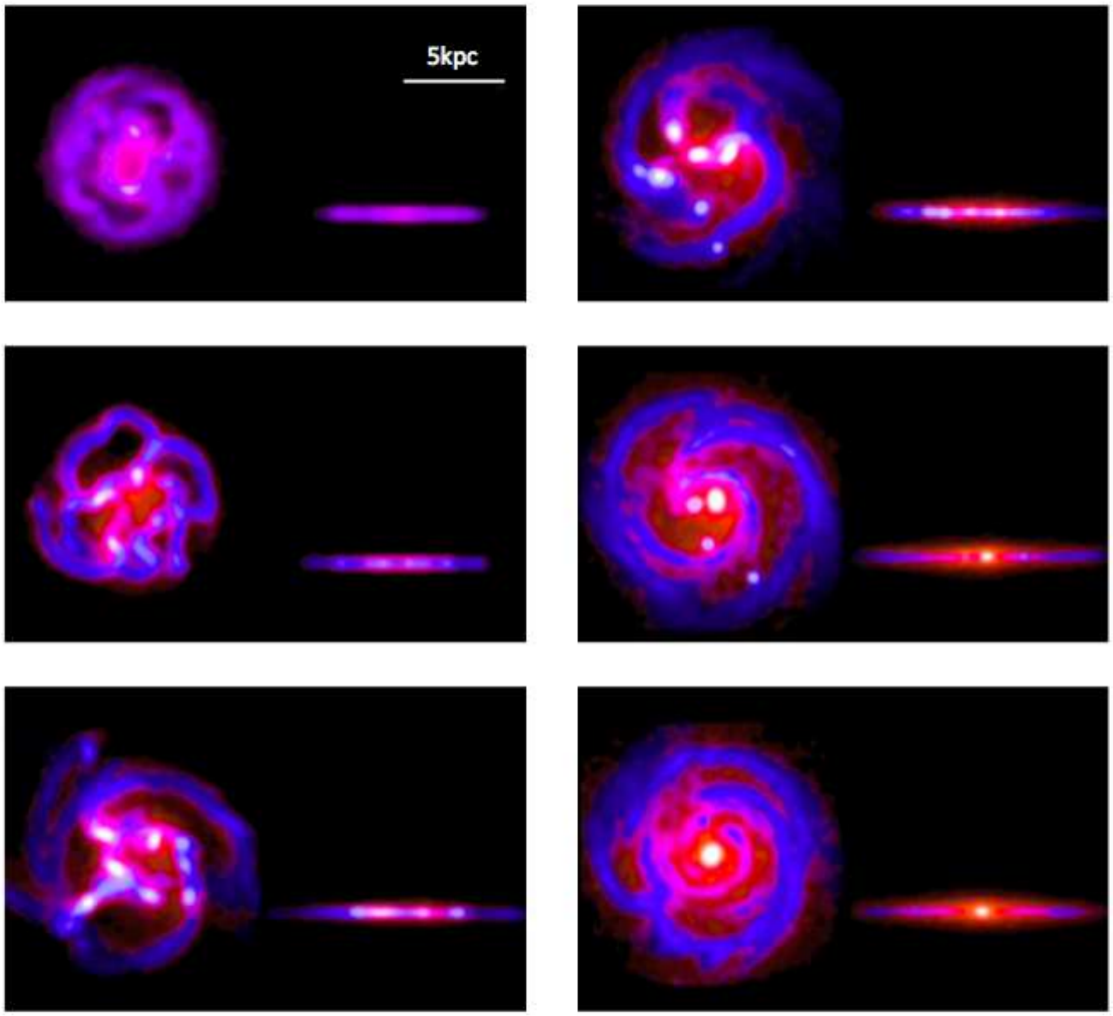

Figure 1.1: *Simulations of a gas-rich (50% gas fraction) disk galaxy with initial parameters representative for star-forming galaxies at $z \simeq 2$. The unstable gaseous disk forms a ring that rapidly fragments into giant clumps. The clumps migrate inward and coalesce into a bulge, while the stellar disk is significantly thickened. The disk radial profile, which is initially flat, is redistributed into an exponential. The bulge formed here is a classical bulge with a Sérsic index of 3.5–4.0. Snapshots are separated by 100 Myr. Gas-dominated regions are in blue, while star-dominated regions are the red ones. Simulation from Bournaud et al.(2007).*

From literature, spheroidals can form via dissipative collapse (e.g. Ballero et al. 2007; McWilliam et al. 2008) with possibly an additional component formed with a time delay of a few Gyrs (e.g. Tsujimoto & Bekki 2012; Grieco et al. 2012), and/or via early mergers of massive clumps (e.g. Immeli et al. 2004; Elmegreen et al. 2008; Bournaud & Elmegreen 2009). In particular, the last theory proposes that galaxy bulges form from the merging of primordial sub-structures, either galaxies embedded in a dark matter halo, or massive clumps generated by early disk instability and fragmentation. The observation at high-redshift of the so-called "chain or clumpy"

galaxies (Elmegreen et al. 2009; Genzel et al. 2011; Tacchella et al. 2015) suggests that the coalescence of primordial substructures is the most promising channel for the formation of bulges so far. Clumpy galaxies are so frequent at $1 \leq z \leq 5$, and the clumps evolve so quickly, that most present-day spirals could have had a clumpy phase in their past.

According to these studies, the clumps may form by gravitational instabilities in gas-rich turbulent disks at the time of galaxy formation. These clumps are characterized by masses of $10^{8-9} M_{\odot}$ and can grow and ignite star formation episodes, leaving a chemical signature. If they resist disruption by star formation, then they interact, lose angular momentum, and spiral to the center in a few dynamical times to form a central bulge component. Unlike the merger of individual galaxies, the clump coalescence leaves a bulge with no specific dark matter component.

While the majority of these massive clumps are predicted to dissolve and form the bulge, a few of them may have survived the total disruption and now broadly appear as globular clusters (Bournaud 2016). At odds with the latter, however, these fossil relics should host multi-iron and multi-age sub-populations, with the same "chemical DNA" of the Bulge. Two stellar systems with such properties were recently discovered in the MW bulge: Terzan 5 and Liller 1 (see Section 1.3 - 1.4). Their characteristics strongly suggest that they could be Bulge Fossil Fragments (BFFs), the remnants of the proto-Bulge formation process.

Thus, as a consequence of this peculiar formation process, a variety of relics tracing different phenomena are expected to populate the Galactic Bulge:

- BFFs,
- in-situ formed genuine GCs,
- accreted genuine GCs, formed in external galaxies,
- nuclear star clusters of cannibalized structures.

The signatures of the different origins are imprinted into the kinematic, photometric and chemical properties of these stellar systems. Each system could provide a new background on the formation history of the Milky Way.

Due to its proximity, the MW Bulge is the only spheroid where individual stars can be observed and where an in-depth study of resolved stellar populations can be conducted. Hence, its investigation is of fundamental importance to probe the early history of the Milky Way assembling.

1.2 Chemical tagging of GCs

Globular clusters are gravitationally bound stellar systems, composed of an average of $10^5 - 10^6$ stars and with a mass of $10^4 - 10^6 M_\odot$. Being very compact objects (the central density can reach n=100-1000 stars per cubic parsec), they are dimensionally small, with a projected diameter of tens of parsecs. For this reason, they are difficult to observe at great distances. Within the Milky Way, globular clusters are distributed in the halo, thick disk and bulge, while they are not present in the thin disk. More than 150 clusters have been observed and catalogued so far (Harris 2010).

The average age of globular clusters in our galaxy is 10-13 Gyr and their stellar populations have turn-off masses of approximately $M_{TO} = 0.8 M_\odot$. They are characterized by old stellar populations and therefore GCs are perfect tracers of the formation history of the MW, and consequently of the formation history of galaxies. In fact, thanks to their chemical tagging, it is possible to identify the nature and the origin of each stellar system with a great level of accuracy. By doing so, the different type of stellar systems can be distinguished and new fragments of the early history of our galaxy can be identified. Hence, it is important to define how to discriminate a globular cluster from another type of stellar system and how to understand its origin from a chemical point of view.

Galactic globular clusters cover a wide metallicity distribution from [Fe/H] ~ -2.5 to [Fe/H] ~ 0.5, and have super-solar [α/Fe] ratio, an indication that stars are born from gas previously enriched mainly by type II Supernovae (SNII). Historically, the scientific community has always considered globular clusters to be the best approximation of Simple Stellar Population (SSP), i.e. an assembly of stars with the same age and the same initial chemical composition, born by a single burst of star formation. However, in the last decades, there have been confirmations of the existence of Multiple Stellar Populations (MSPs) characterized by a large spread in light-element (as Na, Al, O, etc) abundances structured in specific anti-correlations (e.g. Carretta et al. 2009), the most indicative one being the Na-O anti-correlation. Their presence is considered to be one of the main feature characterizing globular clusters, since it has been found to be ubiquitous in all globulars, while it has been found to be absent in field stars, open clusters and BFFs. The origin of these chemical peculiarities is probably due to the pollution of more than one generation of stars over a timescale

of ~ 100 Myr only. Thus, genuine GCs are defined as stellar systems homogeneous in iron and showing significant light-elements spreads; completely different from BFFs and nuclear star clusters, which are instead characterized by multi-iron populations.

The atmospheres of the stars that we observe today keep memory of the chemical composition of the interstellar medium (ISM) from which they formed. In turn, the chemical abundances of the ISM vary in time if more than one burst of star formation occurs, owing to the ejecta of each stellar generation. Thus, stars formed at different times in the same system have different chemical compositions, and by analysing the chemistry of each stellar population one can univocally trace the enrichment process. Different abundance patterns are expected depending on the stars that enriched the ISM and the enrichment timescale. In particular, a few specific abundance patterns are so distinctive that they can be seen as the "chemical DNA" of the stellar population.
This is indeed the case for the [α/Fe]–[Fe/H] diagram (Matteucci & Brocato 1990). The α-elements (like oxygen, magnesium, etc.) are synthesized by massive stars and are released to the ISM over a short time scale (a few million years) by the explosion of core collapse SNe (SNeII). While SNeII also produce a negligible quantity of iron-peak elements, the large majority of these chemical species is the result of explosive nucleosynthesis during the thermonuclear deflagration of a white dwarf in a binary system, in the events known as SNeIa that occur over longer timescales, possibly 1 Gyr (the exact details are still debated in the literature). The injection of such a large amount of iron-peak elements implies that the (initially nearly constant) [α/Fe] ratio set by SNeII starts to sharply decrease when the first generation of SNIa explodes, thus producing the characteristic "knee" in the [α/Fe]–[Fe/H] diagram. The knee therefore flags the metallicity [Fe/H] (due to the action of the sole SNeII) reached by the ISM at the epoch of the explosion of the first generation of SNeIa. This implies that the [α/Fe]–[Fe/H] pattern is a powerful indicator of the star formation efficiency in the environment where the stars formed: the faster a stellar system forms its stars (high star formation rate), the larger is the contribution of SNeII to the chemical enrichment before SNeIa explode, thus the larger is the metallicity of the knee in the diagram.

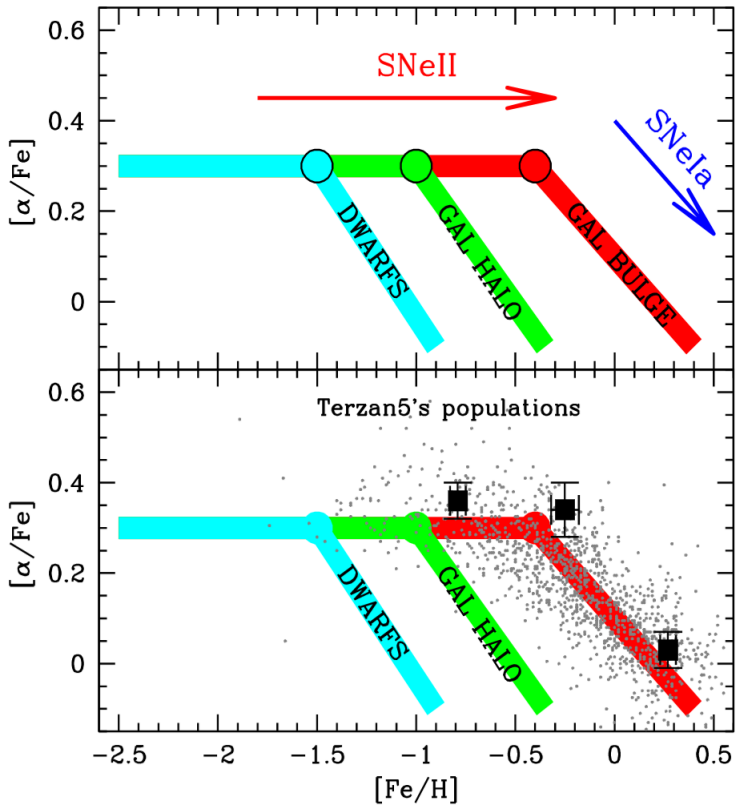

Figure 1.2: *[α/Fe]-[Fe/H] diagram with the schematic representation of the different chemical abundance patterns drawn by dwarf galaxies (cyan line), by the Galactic Halo and Disk (green line) and by the Galactic Bulge (red line). In the second panel, the sub-populations discovered in Terzan 5 are reported (large black dots), together with Bulge field stars from the literature (grey dots).*

Fig. 1.2 schematically summarizes the [α/Fe]–[Fe/H] pattern measured in different structures of the local Universe, demonstrating that, as a chemical DNA, it allows a univocal distinction among them: the chemical DNA of the Galactic Bulge clearly testifies an environment totally incompatible with that of the Halo and the dwarf galaxies, with such a high star formation efficiency that SNeII alone could enrich the ISM up to [Fe/H] $\sim$ –0.3 before the first SNeIa started to explode. The grey dots in the bottom panel of the figure mark the abundances measured in Galactic Bulge stars (Ness et al. 2013; Johnson et al. 2014). The chemical DNA of Terzan 5, as traced by its three stellar populations (Ferraro et al. 2009; Massari et al. 2014; Origlia et al. 2011, 2013), is drawn by the large black squares and manifestly follows the pattern measured in the Bulge. As shown in the figure, this DNA is not common in the Local Group. It requires quite special conditions and can be considered as a univocal signature of stellar populations of the Galactic Bulge. This is a clear example of how the result of this DNA test is indisputable: Terzan 5 and the Galactic

Bulge experienced the same overall chemical enrichment history.

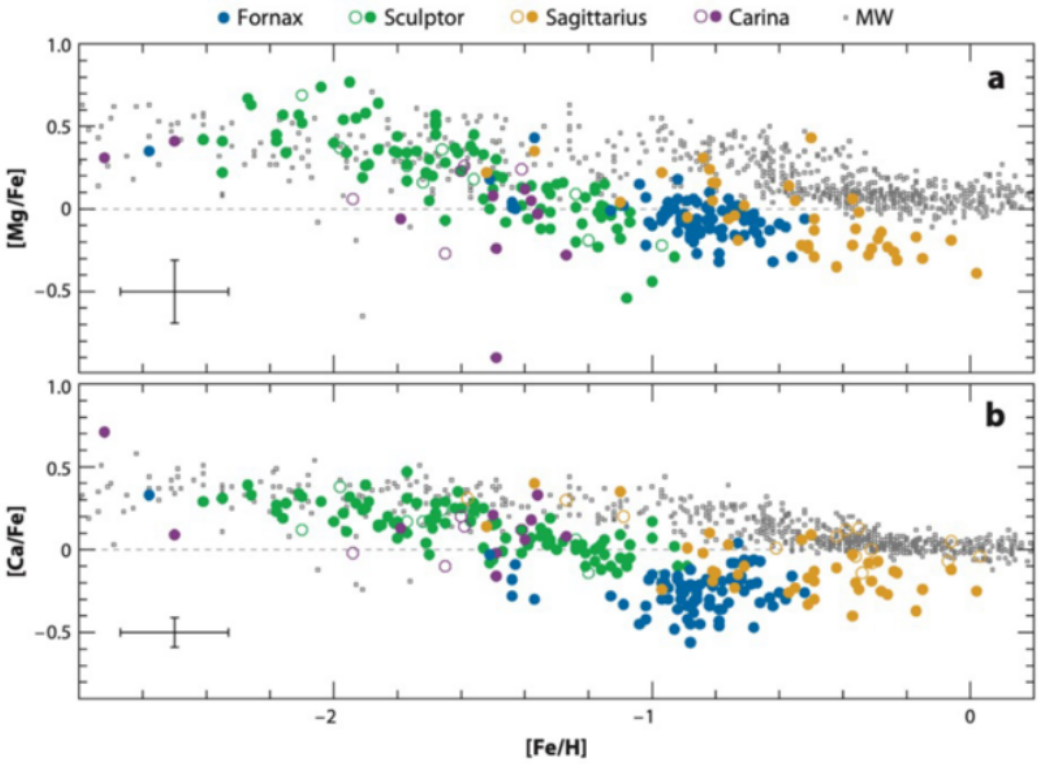

Figure 1.3: *Two α-elements (Magnesium and Calcium) as a function of [Fe/H] in four nearby dwarf spheroidal galaxies: Sagittarius (orange: McWilliam & Smecker-Hane 2005; Monaco et al. 2005; Sbordone et al. 2007), Fornax (blue: Shetrone et al. 2003; Letarte 2007), Sculptor (green: Shetrone et al. 2003; Geisler et al. 2005), and Carina (purple: Shetrone et al. 2003; Koch et al. 2008). The small grey dots are from a compilation of the MW Disk and Halo stars (Venn et al. 2004). From Tolstoy et al. 2009.*

At the same time, the Halo and Disk (Chiappini et al. 1999; Matteucci & Chiappini 2005) show a chemical DNA completely different from that of nearby smaller galaxies (Lemasle et al. 2012). The knee of the [α/Fe] pattern in dwarf galaxies occurs at a metallicity sensibly smaller ([Fe/H]$\sim$ -1.5) than in the MW Halo and Disk ([Fe/H]$\sim$ -1.0), indicating an environment with a much less efficient SFR. This is also shown in Figure 1.3, where the abundance patterns of various nearby dwarf spheroidal galaxies are compared with that of the Milky Way (from Tolstoy et al. 2009). All show a much lower SFR than that of our galaxy, confirming the usefulness of this "chemical DNA test". Thanks to it, indeed, one can differentiate between in-situ formed genuine GCs and accreted genuine GCs formed in an external galaxy.

The classical [α/Fe]-[Fe/H] diagram is obviously the most tested and used "DNA test", but it is not the only one. Alternative abundance patterns have been recently proposed, showing that also iron-peak elements, as Vanadium (V), Scandium (Sc) and Zinc (Zn) can be powerful indicators of the environment where stars formed (Minelli et al. 2021b; Mucciarelli et al. 2021). These elements are mainly produced in high-mass ($\geq$ 20) stars, as a result of the explosion of hypernovae, SNeII and electron-capture SNe (Romano et al. 2010; Kobayashi et al. 2020). As a result, the Fe-peak elements abundance ratios are expected to be larger in high SFR environments, where massive star production is greater, than in low SFR systems, as in dwarf galaxies (Yan et al. 2017; Jeřábková et al. 2018). Thanks to this new chemical DNA test it is possible to differentiate between a genuine globular cluster formed in our galaxy and an accreted one previously belonging to a stellar system that experienced a different SFR, as in a nearby dwarf galaxy of the Local Group. One of the first application of this new generation of DNA tests has yielded very intriguing results, by revealing the possible extra-Galactic origin of two metal-rich GCs in the Bulge direction (namely, NGC6441 and NGC6388). This is shown in Figure 1.4 from Minelli et al. 2021b, where Silicon, Vanadium and Zinc abundance ratios of four metal-rich Galactic GCs are compared. These GCs are located in the metallicity range ([Fe/H]$\sim$ -0.5 dex) where the iron-peak element abundance ratios should exhibit the largest discrepancy in case of different origin (Minelli et al. 2021a). While the [Si/Fe] measures of the 4 clusters are fully consistent with those of Sagittarius (Sgr), Large Magellanic Cloud (LMC) and MW field stars, the [V/Fe] and [Zn/Fe] measure show a discrepancy. As can be appreciated in this diagram, the MW stars appears clearly distinct from the SGr and LMC ones. Moreover, the [V/Fe] and [Zn/Fe] abundances of NGC6441 and NGC6388 are significantly lower (by $\sim$ 0.5 dex) than those measured in the other two MW GCs with similar metallicity (namely, NGC 5927 and NGC 6496), and well consistent with the values measured in the Large Magellanic Cloud and Sagittarius. The low abundance of these iron-peak elements in LMC/Sgr stars is interpreted as due to a lower contribution from massive stars to the chemical enrichment, compared to that experienced by the MW. Hence, although based on just a few stars, this evidence yields to the conclusion that NGC6388 and NGC6441 are not in-situ formed clusters, but possibly the result of one of the merging events suffered by the MW in its past. It is important to emphasise that these new complementary DNA tests have been found to be particularly effective in distinguishing GCs formed in relatively metal-rich extra-

Galactic environments (as particularly massive dwarf or irregular galaxies, like Sgr and LMC), where more commonly investigated abundance ratios lose their sensitivity as a proxy of different stellar birth places. In fact, it is worth of noticing that the abundance of Silicon (one of the widely used α-elements) is essentially the same in Sgr, LMC and MW stars (see the top panel of Fig. 1.4), while both the [Zn/Fe] and [V/Fe] ratios are able to clearly separate stars belonging to the Sgr and LMC, from those of the MW (see also Skúladóttir et al. 2017).

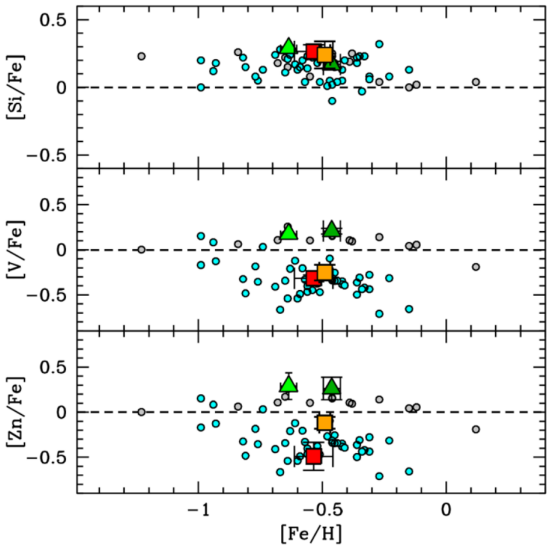

Figure 1.4: *[X/Fe] abundance ratios of Silicon, Vanadium and Zinc measured in four metal-rich Galactic GCs: NGC6496 (light green triangle), NGC5927 (dark green triangle), NGC6441 (red square) and NGC6388 (orange square). In the background, the abundance ratios of MW stars (grey circles) and of LMC and Sgr dwarf galaxy stars (cyan circles) are reported.*
Data from Minelli et al. 2021b.

1.3 The first peculiar object: Terzan 5

As already mentioned above, the "merging picture" for the formation of the Bulge opens the possibility that not all the massive clumps have actually dissolved and that some of them are still present in the inner regions with the appearance of massive GCs (Bournaud 2016). But unlike a genuine globular cluster, these fossil relics should have been massive enough to retain the ejecta of SN explosions, and possibly experienced multiple burst of star formation.
The first candidate, a massive ($2 \cdot 10^6 M_\odot$) GC named Terzan 5, was identified back in 2009 (Ferraro et al. 2009). Terzan 5 is located at 5.9 kpc from the Galactic center

and it has an average E(B-V) $\sim$ 2.5 mag and an extinction variations as large as δE(B-V) $\sim$ 0.67, especially in the direction of the center of the system (Massari et al. 2012). Its detailed photometric and spectroscopic study (Ferraro et al. 2009; Origlia et al. 2011; Massari et al. 2014; Ferraro et al. 2016) has revealed the presence of at least two major sub-populations, associated to different star formation events in a self-enrichment scenario. The first major and short-lived ($\leq$ 1 Gyr) burst occurred about 12 Gyr ago, at the epoch of Galaxy assembling, with sub-solar metallicity ([Fe/H] $\approx$ -0.3) and enhanced [α/Fe] $\approx$ +0.4 abundance ratio. The second star formation burst, instead, occurred $\sim$ 4.5 Gyr ago (approximately 7.5 Gyr later) from gas with super-solar metallicity peaking at [Fe/H] $\approx$ +0.3 and solar-scaled [α/Fe]. A third, minor metal-poor population, seems also to be present with [Fe/H] $\approx$ -0.79 and [α/Fe] $\approx$ +0.36 (Origlia et al. 2013). After the formation of two old components, Terzan 5 experienced a long phase of quiescence during which the gas ejected from both SNeII and SNeIa accumulated in the central region, to form the young super-solar population. This requires the Terzan 5 ancestor to be quite massive (at least a few $10^8 M_{\odot}$; Baumgardt et al. 2008), enough to retain the large amount of gas before igniting the second burst of star formation. The hypothesis of self-enrichment, i.e the metal-richer component formed from gas enriched in iron by the ejecta of the previous, metal-poorer, population, is not only supported by the observed chemical patterns but also by the observed radial distributions of the different sub-populations. In fact, the metal rich component has been found to be significantly more centrally concentrated that the metal-poor one, as expected in the self-enrichment scenario (Ferraro et al. 2009; Lanzoni et al. 2010; Massari et al. 2015).

Figure 1.5 shows the Terzan 5 proper-motion selected (K, I-K) Colour-Magnitude Diagram (CMD), with highlighted the presence of two distinct Main Sequence Turn-Off (MS-TO) and Sub-Giant Branches (SGBs), indicative of two stellar sub-populations with different ages.

These results definitively exclude the possibility that Terzan 5 is a genuine globular cluster. In fact, apart from the overall morphological appearance, Terzan 5 shares no other property with globulars. It displays a completely different enrichment history and age spread of the sub-populations (the enrichment timescale in GCs is of a few 10^8 years, so their light-element sub-populations are almost coeval; D'Ercole et al. 2008) and at odds with genuine clusters, its must be associated to a much more massive progenitor (able to retain the high-velocity SN ejecta). Additionally,

GCs show inhomogeneities only in the light-elements (Carretta et al. 2009), while Terzan 5 presents a significant iron spread (Δ[Fe/H] $\sim$ 1 dex) and no evidence of light-element abundance patterns.

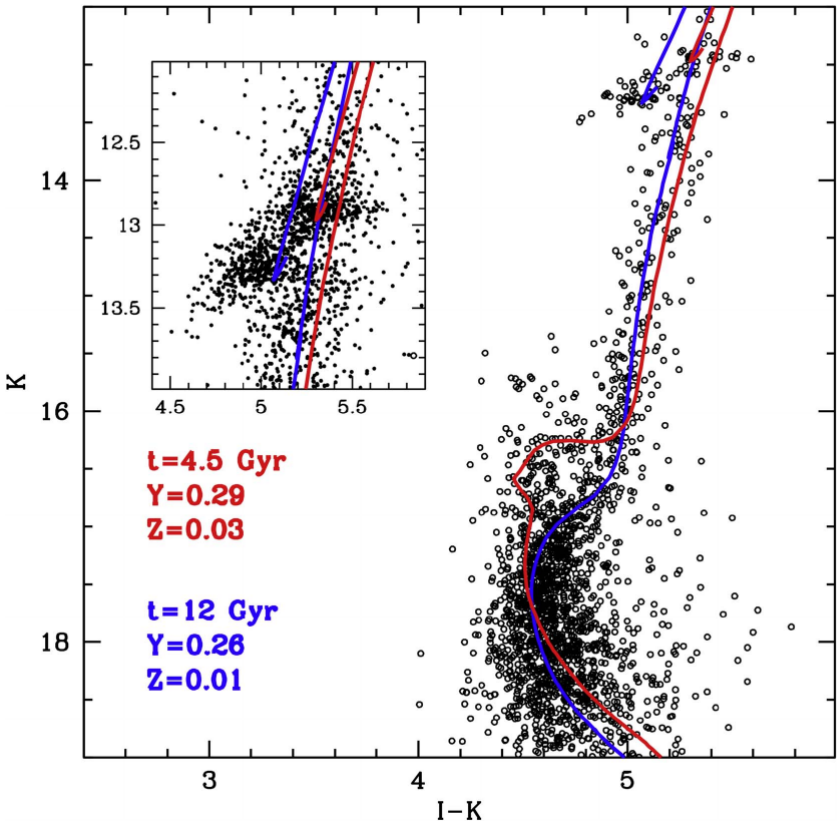

Figure 1.5: *Differential reddening corrected (K, I–K) CMD of Terzan 5 obtained by combining the deepest VLT-MAD K-band and HST-ACS I-band images of a relatively small ($\sim$ 600 arcsec^2) region, where differential reddening is the least and the most homogeneous. The CMD clearly shows the presence of two distinct stellar sub-populations (notice the zoom of the double red clump region). The blue line traces the 12 Gyr old isochrone of the metal-poor population, while the red line traces the younger 4.5 Gyr isochrone of the metal-rich population. The parameters of the chosen isochrones are shown in the lower left. From Ferraro et al. 2016.*

The most important confirmation of the nature of Terzan 5 comes from the chemical tagging of its stellar populations. The [α/Fe]-[Fe/H] diagram drawn by its sub-populations is perfectly consistent with that of Bulge field stars, while it is incompatible with those of the MW Halo and Disk and Local Group dwarf galaxies (Fig. 1.2). So, not only the iron abundance, but also the amount of α-enhancement and its dependence on metallicity are fully consistent with those measured in the Galactic bulge. This "chemical DNA test" unambiguously links Terzan 5 with the Bulge and strongly supports an in-situ origin.

Moreover, its radial velocity and proper motions from HST (Massari et al. 2015) and Gaia (Baumgardt et al. 2019; Massari et al. 2019) allowed to reconstruct its orbit with an apocenter of 2.8 kpc, confining its formation and evolution within the Bulge.

The observational evidences collected so far leave almost no doubts on the interpretation of Terzan 5 as a candidate remnant of one of the massive clumps that contributed to generate the Milky Way Bulge. However, the discovery of other similar fossil survivor is fundamental to better understand the Bulge formation and introduce in the literature a new class of stellar systems: the Bulge Fossil Fragments.

1.4 A recent discovery: Liller 1

New perspectives about the existence of the BFF class were opened by the discovery of another GC-like stellar system in the Bulge (Liller 1) hosting multi-age and multi-iron subpopulations (Ferraro et al. 2021a).

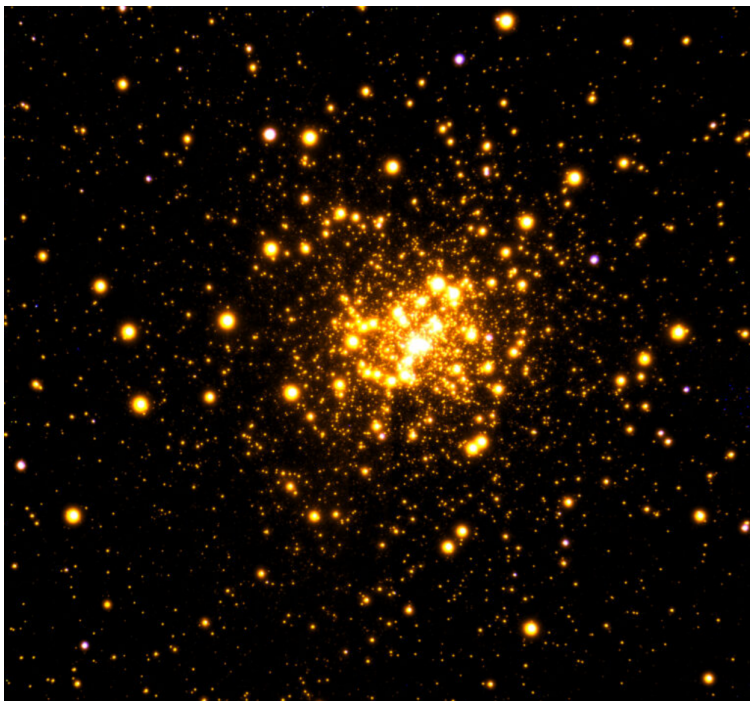

Figure 1.6: *Close-infrared image of the globular cluster Liller 1 obtained with the GeMS adaptive optics system of the Gemini South telescope at the Gemini Observatory in Chile.*

Liller 1 is located in the innermost region of the Galaxy at only 0.8 kpc from the MW center, very close to the Galactic plane (at Galactic longitude $l = 354.84°$ and

latitude $b = -0.16°$; Harris 1996), in a region largely affected by variable extinction. Liller 1 is located in a region even more obscured than Terzan 5, with an average E(B-V) color excess of ≈ 4.5 mag and differential reddening δE(B-V) between -0.57 and 0.37 (Pallanca et al. 2021). This is clearly the reason why it has remained unexplored for so long.

Liller 1 is also particularly massive, with an estimated mass of $M_{TOT} = 1.5 \times 10^6 M_\odot$ (Saracino et al. 2015), and it is characterized by a high collision rate as Terzan 5 (Verbunt & Hut 1987). This suggests that this cluster may also contain a large number of millisecond pulsar (MSPs). In particular, the strong gamma-ray emission measured by the Large Area Telescope (LAT) on board Fermi (Tam et al. 2011) could be explained by an elevated presence of MSPs inside.

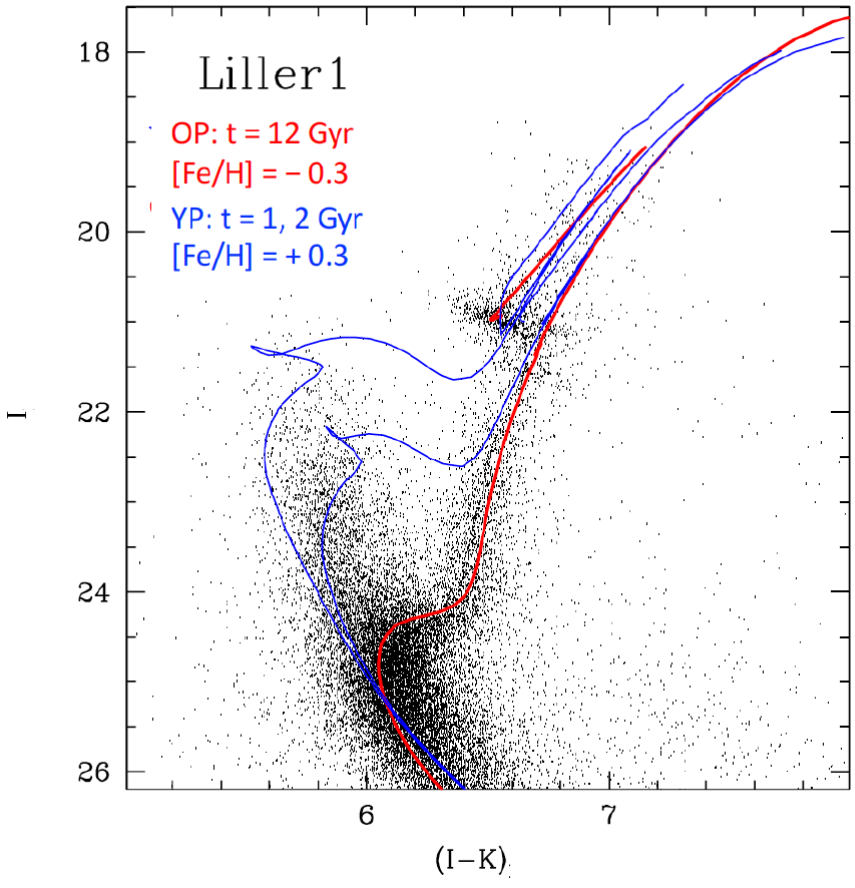

Figure 1.7: *Proper motion-selected and differential reddening-corrected (I, I-K) CMD of Liller 1, with the isochrones used to derive the ages of its old (red line) and young (blue line) sub-populations.*

The PM-selected and differential reddening-corrected optical-NIR CMD of Liller 1, obtained from the combination of I and K band images acquired with the Hubble

Space Telescope (HST) and the Gemini South Adaptive Optics Imager (GSAOI) camera is shown in Fig 1.7. It has revealed the presence of two distinct sub-population with remarkably different ages. The oldest one is very similar to that observed in Terzan 5 with an age around 12 Gyr and a sub-solar metallicity, while the younger component (appearing as a sort of "blue plume" extension of the main sequence) is only 1-3 Gyr old, probably and possibly with super-solar metallicity (Ferraro et al. 2021a). A further confirmation that the blue plume belongs to Liller 1 comes from the radial distribution that shows that it is even more centrally concentrated than the old population.

The isochrones of different age and metallicity reproducing the position of the two main sub-populations in the CMD are shown in Figure 1.7. To match the main old sub-population, a 12 Gyr old isochrone with metallicity $[Fe/H] \approx -0.3$ dex was selected, as the one used to represent the metal-poor population of Terzan 5 (see also Fig. 1.5). To reproduce the young sub-population, instead, three young isochrones of 1, 2, and 3 Gyr, at a super-solar metallicity $[Fe/H] \approx +0.3$ dex are reported.

Such a high-quality CMD has been also used to model the Liller 1 star formation history (SFH), an important piece of information to assess its origin. The best-fit solution reveals that star formation was active in Liller 1 over its entire lifetime, with three broad episodes (Dalessandro et al. 2022a). The dominant burst of SF occurred $\approx$ 12-13 Gyr ago with a tail extending for $\sim$ 3 Gyr, creating an old population which contributes to about 70% of the total stellar mass. The intermediate episode occurred between 6 and 9 Gyr ago, while the most recent one took place between 1 and 3 Gyr ago. The remaining fraction of the total stellar mass is almost equally split between the latter ($\approx$ 15% for the intermediate one and $\geq$ 10% for the younger). These results suggest that Liller 1 unlikely formed through the recent merger between an old and massive GC and a giant molecular cloud (GMC), as recently proposed (McKenzie & Bekki 2018; Bastian & Pfeffer 2022), because this kind of scenario will produce two discrete and well-separated SF episodes. On the contrary, its complex SFH provide further support to the idea of Liller 1 as a surviving relic of a massive primordial structure.

Obviously, spectroscopic confirmation of the existence of these multi-age and multi-iron population is required. The first high-resolution IR spectroscopic study of Liller 1 has been performed using the Near InfraRed Spectrograph (NIRSPEC) at the Keck Observatory for two of the brightest giants belonging to the metal-poor population. As photometrically assumed, this study suggests that its old population

has a chemistry fully compatible with the one of the old population of Terzan 5; in particular, [Fe/H] ≈ -0.3 dex and [α/Fe] ≈ +0.3 dex (Origlia et al. 2002). Recently, the first Liller 1 metallicity distribution has been derived from low resolution spectra obtained with the Multi Unit Spectroscopic Explorer (MUSE) in the Ca triplet region (Crociati et al. 2023), showing a dominant metal-poor component with a peak at [Fe/H] ≈ -0.5 dex and a metal-rich component with a peak at [Fe/H] ≈ +0.3 dex (with a 1σ dispersion of about 0.2 dex). Other spectroscopic campaigns, performed at medium ($R \sim 8000$) and high ($R \sim 25000$) spectral resolution by using, respectively, X-shooter (Alvarez Garay et al. 2024) and NIRSPEC (Fanelli et al. 2024), fully confirmed the expectations, finding a clear bimodal distribution with a sub-solar and a super-solar component (Fig. 1.8).

The NIRSpec study has also statistically assessed the presence of a third sub-component with iron content and [α/Fe] enhancement somewhat intermediate between the metal-poor and metal-rich sub-populations. This provides the chemical signature of an extended star formation with multiple bursts and of some self-enrichment, like predicted by the reconstructed star formation history of the system (Dalessandro et al. 2022a). Although more statistics is needed to firmly establish whether this third component is truly a distinct sub-population, this finding represents an important step in the identification of the origin of Liller 1. Indeed, it offers the observational evidence that this stellar system cannot be explained by a genuine globular cluster accreting a giant molecular cloud, as previously mentioned, or by the simple merging of two genuine GCs (Khoperskov et al. 2018; Mastrobuono-Battisti et al. 2019; Pfeffer et al. 2021), since its age, metallicity and [α/Fe] distributions are clearly more complex.

A detailed chemical analysis of an expanded sample of Liller 1 stars based on higher resolution spectroscopy ($R \sim 50,000$) is currently ongoing at the ESO-VLT with the spectrograph CRIRES+ in the context of the "Bulge Cluster Origin" (BulCO) survey (see Section 2.1). This sample will allow to increase the statistics of the distribution, especially in the least populated region of the [α/Fe]-[Fe/H] diagram around solar metallicity, thus solidly constraining Liller 1 nature spectroscopically and increasing our knowledge of this curious object.

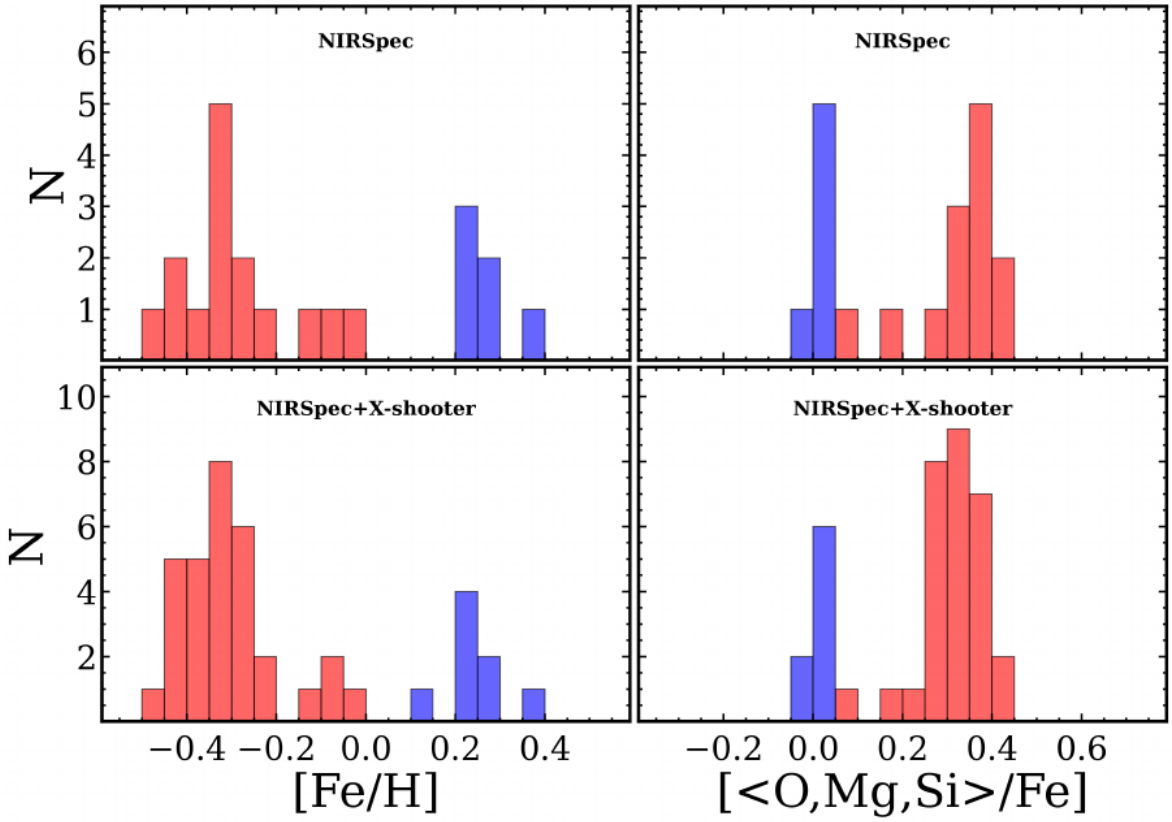

Figure 1.8: *Histograms of the [Fe/H] and [<O,Mg,Si>/Fe] abundance measurements (left and right panels, respectively) obtained in Fanelli et al. 2024 from the analysis of NIRSpec spectra alone (top panels), and in combination with the sample from Alvarez Garay et al. 2024 (bottom panels). The sub-solar and super-solar components are shown in red and blue, respectively. From Fanelli et al. 2024.*

Chapter 2

Database

2.1 The BulCO survey

This work is inserted into a larger project: the Bulge Cluster Origin (BulCO) survey (Ferraro et al. 2024, in preparation). The BulCO survey aims at performing an unprecedented high-resolution chemical screening of the stellar populations in a substantial sample of representative Bulge stellar systems, searching in each of them a fragment of the early history of our galaxy. This is achieved taking advantage of the pioneering experience in near-infrared (NIR) spectroscopy of star clusters acquired by the Bologna stellar group over the years (Origlia et al. 1997, 2002, 2003; Origlia & Rich 2004; Origlia et al. 2005, 2008), along with the enhanced capabilities of the NIR spectrograph CRIRES+ at the Very Large Telescope (VLT). The BulCO survey is part of a comprehensive project aimed at the detailed characterization of Bulge stellar systems, with the ultimate goal of reconstructing the evolutionary history of the MW Bulge. The spectroscopic observations of the survey are combined with high-resolution and multi-wavelength photometric observations, proper motion (PM) membership selection, and precise differential reddening correction (e.g. Massari et al. 2012; Saracino et al. 2015, 2016, 2019; Pallanca et al. 2021, 2023; Libralato et al. 2022; Cadelano et al. 2023; Deras et al. 2023).

As discussed in the previous chapter, according to the current view of the cosmic structure formation, a variety of relics tracing different phenomena are expected to populate the bulge: the remnants (possibly the nuclei) of the primordial massive clumps that contributed to the bulge formation (BSS), in-situ formed and externally accreted globular clusters (GCs), and also nuclear star clusters of cannibalized galaxies. The signatures of different origins are imprinted in the observable

properties of these stellar systems. In particular (as discussed in Chapter 1) the chemistry is a powerful tool, since stars that formed at different times and with varying star formation rates (SFRs) possess distinct chemical compositions. Consequently, analysing the chemistry of each stellar population allows for the univocal tracing of the enrichment process of the ISM in which the stars formed. Different abundance patterns are expected for stellar systems formed in environment enriched with different timescales and efficiency as schematically detailed below:

1. BFFs should host multi-iron and multi-age sub-populations, with the same "chemical DNA" of the Bulge;

2. nuclear star clusters of cannibalized structures are expected to show iron spread and specific abundance patterns substantially different from the bulge, tracing instead the environment where they formed (the halo or any dwarf galaxy);

3. genuine GCs should be homogeneous in iron and present peculiar light-elements correlations and anti-correlations (Carretta et al. 2009, 2010; Milone et al. 2017); in-situ formed and accreted GCs are distinguished using their α and iron-peak abundance patterns.

The selected spectroscopic targets for the BulCO survey are 17 stellar systems in the MW Bulge, chosen with the specific aim of decoding their chemical DNA and unveil their true origin. The target list includes stellar systems that at the present time are suspected to belong to different "categories": the two currently known BFFs (Terzan 5 and Liller 1); the two most metal-rich and mono-metallic GCs in the MW (NG6553 and NGC6528); the two most massive Bulge star cluster, suspected to be accreted systems (NGC6388 and NGC6441; Minelli et al. 2021b; Carretta & Bragaglia 2023); NGC6656, a globular cluster suspected to host multi-iron sub-populations (Marino et al. 2009; Mucciarelli et al. 2015); an almost chemically unexplored sample of stellar systems in the inner Bulge (i.e NGC6380, NGC6304, NGC6316, Terzan 1, Terzan 2, Terzan 6, Terzan 10, Palomar 6, UKS1, Djorgovski2).

Cluster Name	M_V [mag]	E(B-V) [mag]	[Fe/H] [dex]	Core radius [arc min]
NGC6304	-7.3	0.5	-0.45	0.21
NGC6316	-8.3	0.5	-0.45	0.65
NGC6380	-7.5	1.2	-0.75	0.34
NGC6388	-9.4	0.4	-0.55	0.12
NGC6441	-9.6	0.5	-0.46	0.13
NGC6528	-6.6	0.5	-0.11	0.13
NGC6553	-7.8	0.6	-0.18	0.53
NGC6656	-8.5	0.3	-1.70	1.33
Palomar 6	-6.8	1.5	-0.91	0.66
Terzan 1	-4.4	2.0	-1.03	0.04
Terzan 2	-5.9	1.9	-0.69	0.03
Terzan 5	-7.4	2.3	-0.23	0.16
Terzan 6	-7.6	2.3	-0.56	0.05
Terzan 10	-6.3	2.4	-1.00	0.90
UKS1	-6.9	3.1	-0.64	0.15
Djorgovski 2	-7.0	0.9	-0.65	0.33
Liller 1	-7.3	3.1	-0.33	0.06

Table 2.1: *Main properties of the 17 selected target clusters.*

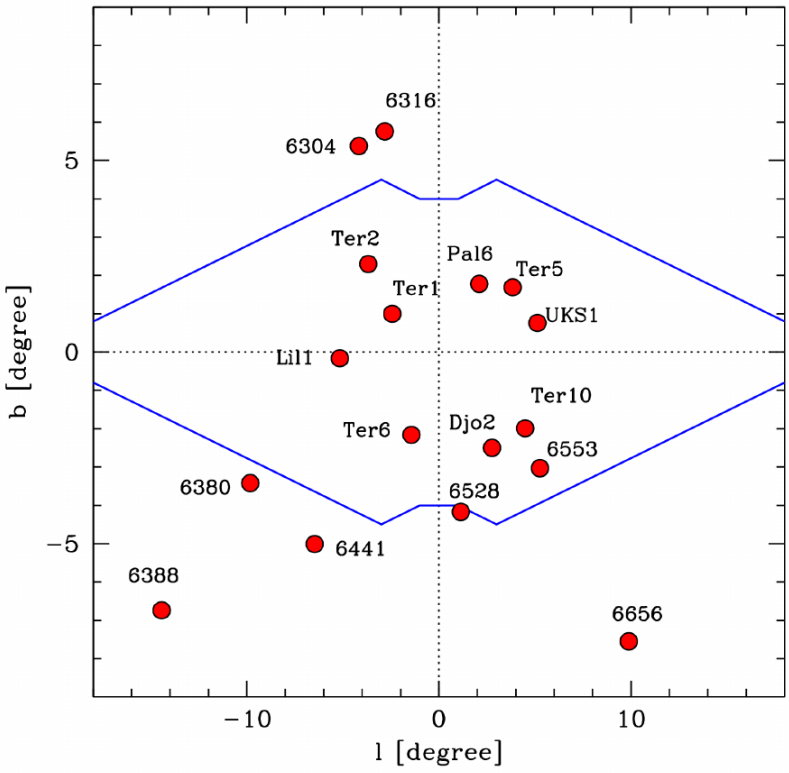

Figure 2.1: *Position of the 17 selected clusters (large red circles) for the BulCO survey in Galactic longitude (l) and latitude (b). The blue lines stand for the outline of the inner Bulge as traced at 3.5 µm by COBE/DIRBE (Weiland et al. 1994).*

The main properties of the mentioned targets and their position in Galactic longitude and latitude coordinates are shown in Table 2.1 and Figure 2.1 respectively.
The BulCO survey will sample at least 20 giants in each system. As detailed below, the sample has been selected from photometric catalogs of members selected on the basis of PMs and radial velocity from previous observations. This is indeed the minimum sample needed to recognize the possible presence of sub-populations as small as 25% of the total. Indeed, under the hypothesis of random sampling, such a component would contribute with $\sim$ 5 stars, which is the least possible number to statistically certify the presence of any sub-population. To select these stars in each cluster, large photometric dataset collected over the years both in the NIR and in the optical bands have been used (Ferraro et al. 2000, 2009, 2021a; Valenti et al. 2005, 2007; Lanzoni et al. 2007, 2010, 2013; Pallanca et al. 2021). This dataset was complemented by ongoing HST and GEMINI observations, as well as archive images regained from the GEMINI, VLT and HST repositories. As far as possible, relative PMs have been calculated by using multi-epoch HST images (Libralato et al. 2022) or by combining HST and adaptive optics assisted ground-based images (e.g. Ferraro et al. 2016, 2021a; Dalessandro et al. 2016, 2022a). Moreover, PM measurements from GAIA DR3 (Gaia Collaboration et al. 2016, 2023) and accurate radial velocity obtained from the ongoing spectroscopic survey MIKiS (Ferraro et al. 2018) have been taken into account. More than 450 observing blocks have been submitted for execution to ESO, corresponding to a total amount of 420 giants in the 17 target clusters. For the chemical screening of these highly reddened systems, each giant has been observed in at least two of the three selected gratings of CRIRES+ (J1126, H1582, K2166). These gratings sample a large number of unblended spectral lines, which are crucial for the construction of the necessary chemical DNA tests in each system:

- the J1226 grating allows to measure the abundance of Iron (35 lines); iron-peak elements: Zinc (at 1305.3 nm), Vanadium (4 lines), Chromium (14 lines), Cobalt (at 1272.0 nm and 1163.1 nm), Nickel (5 lines), Manganese (at 1341.5 nm); α-elements: Calcium (13 lines), Silicon (25 lines), Magnesium (5 lines), Titanium (19 lines); other light elements: Carbon (CI triplet at 1175 nm), Nitrogen (from a few dozen CN molecular lines), Sodium (at 1138.1 nm, 1140.3 nm and 1231.1 nm), Aluminium (at 1312.3 nm and 1315.0 nm), Potassium (4 lines);

- the H1582 grating allows to add fundamental measurements of Oxygen and $^{12}C+^{13}C$ abundances from a few dozen OH and CO molecular lines, respectively, Sulphur (at 1548.2 nm and 15474.0 nm), a few ionized lines of the Cerium (6 lines), as well as other lines of V (at 1592.5 nm), Fe (64 lines), Cr (2 lines), Mn (2 lines), Ni (12 lines), Co (2 lines), C (5 CI lines), Mg (3 lines), Si (6 lines), Ca (4 lines), Ti (4 lines), Na (one line), Al (3 lines) and N (a few dozen CN molecular lines);

- the K2166 grating, covering the 2150-2280 nm spectral region, allows the detection of about 12 iron and 25 α-element lines (Mg, Si, Ti, Ca and S).

By combining the abundance measures obtained from the different gratings, it is possible to constrain the cluster formation scenario, enrichment timescale and stellar nucleosynthesis for every target. In particular, the following chemical diagnostics are the most significant:

- The [Fe/H] distribution within each cluster is fundamental to immediately distinguish between a genuine GC with a single-iron population and a more peculiar object, such as a potential BFF or a nuclear star cluster.

- The [iron-peak/Fe] abundance ratios of V, Sc and Zn may be used to discriminate between an in-situ Bulge origin (solar-scaled, e.g. Lomaeva et al. 2019) and an extra-Galactic origin (significantly depleted values, e.g. Minelli et al. 2021b).

- The [α/Fe] abundance ratios provide essential constraints to distinguish between in-situ (Bulge) and external (Galactic Halo and Disk or extra-Galactic) formation scenarios. In addition, the α-elements abundance measures furnish crucial information on the relative contribution and timescale of SNII and SNIa enrichment of the gas.

- CO and OH molecular lines are critical thermometers to correctly estimate the star surface temperature (T_e), a fundamental stellar parameter for the chemical analysis.

- The O, Na, Al, Mg and K abundance distributions within each cluster are necessary to determine whether there has been self-enrichment in light-elements organized in the typical anti-correlations. Their presence is one of the main features of a genuine GC.

- The [C/N] and $^{12}C/^{13}C$ abundance ratios are robust tracers of the mixing and extra-mixing processes during the RGB evolution.

2.2 The instrument: CRIRES+

The BulCO survey was specifically designed to take advantage of the improved performances of the CRyogenic high-resolution InfraRed Echelle Spectrograph (CRIRES+) operating at the Very Large Telescope of the European Southern Observatory (ESO VLT) at Cerro Paranal (Chile). The spectroscopic observations have been carried out under Large Program 110.24A4 (PI: Ferraro) granted with 255hr of observing time.

Figure 2.2: *The Very Large Telescope (VLT) site, Mount Paranal, Chile.*

The VLT is the most sophisticated optical instrument in the world, comprising four principal telescopes (Unit Telescopes, UT) with primary mirrors measuring 8.2 metres in diameter and four mobile auxiliary telescopes (Auxiliary Telescopes, AT) with 1.8 metres mirrors. Its instrumentation programme represents one of the most ambitious undertaking ever conceived for a single observatory. It encompasses a diverse array of instruments, including wide-field imagers, adaptive optics-corrected cameras and spectrographs, as well as high-resolution and multi-object spectrographs. The VLT instrumentation spans a wide region of the electromagnetic spectrum, from

the far ultraviolet (300 nm) to the mid-infrared (24 μm).
The telescopes are capable of functioning together to form a giant 'interferometer', the ESO Very Large Telescope Interferometer (VLTI), but they can also operate individually. With one of the 8.2m diameter Unit Telescopes, images of celestial objects as faint as magnitude 30 can be obtained in a one-hour exposure. This is made possible by the recently developed adaptive optics system. In contrast to conventional adaptive optics systems, which are only capable of correcting a limited portion of the visible sky, typically 15", the VLT system is capable of addressing a significantly larger region of the sky.

CRIRES+ is a cross-dispersed infrared echelle spectrograph located at the Nasmyth B focus of UT3. It is an upgraded version of the original/old CRIRES (oCRIRES) instrument, which was in operation from 2006 to 2014 at the UT1 of the VLT. The cross-dispersion of the spectrum is performed by the use of reflection gratings; more specifically six gratings, mounted on a cryogenic wheel. Each of them is optimized for operation in a single wavelength band (Y, J, H, K, L and M). An echelle spectrograph is a type of spectrograph specifically optimized for high-resolution spectroscopy, that maximizes the simultaneously covered wavelength range ($COVERAGE = \delta\lambda \cdot N_{pixel}$). Unlike the long slit spectroscopic configuration, the echelle one rearrange the light on the array by dividing the spectrum in several small spectral regions (several "strips", the so-called "orders"). The entire spectral coverage is obtained by merging together all the orders. This design allows for a large range of wavelengths to be simultaneously recorded on the detector, providing detailed spectral information with exceptional resolving power. CRIRES+ provides a spectral resolution of 50,000 (0.4" slit) or 100,000 (0.2" slit) in the spectral range from 0.95 to 5.3 μm. The slit length projected on sky is 10". Adaptive Optics (MACAO - Multi-Applications Curvature Adaptive optics) is used to feed the light into the slit and thereby enhance the signal-to noise ratio (SNR) of the observations. The detector array, composed of three Hawaii 2RG detectors, will span 6144 x 2048 pixels (111mm x 37mm) at a pixel size of 18μm.
By varying the echelle angle and the cross-disperser grating, CRIRES+ is able to fully cover each Y, J, H, K, L, M photometric band (see Figure 2.3) with a small number of configurations. The number of required exposures depends on the particular band; however, fewer exposures are needed to cover the shorter wavelength regions. In particular, two settings are sufficient to fully cover the Y band, while

three settings are needed to fully cover the J band and four settings are required to cover the H and K bands. Several settings are needed to achieve complete coverage of the mid-IR L and M bands.

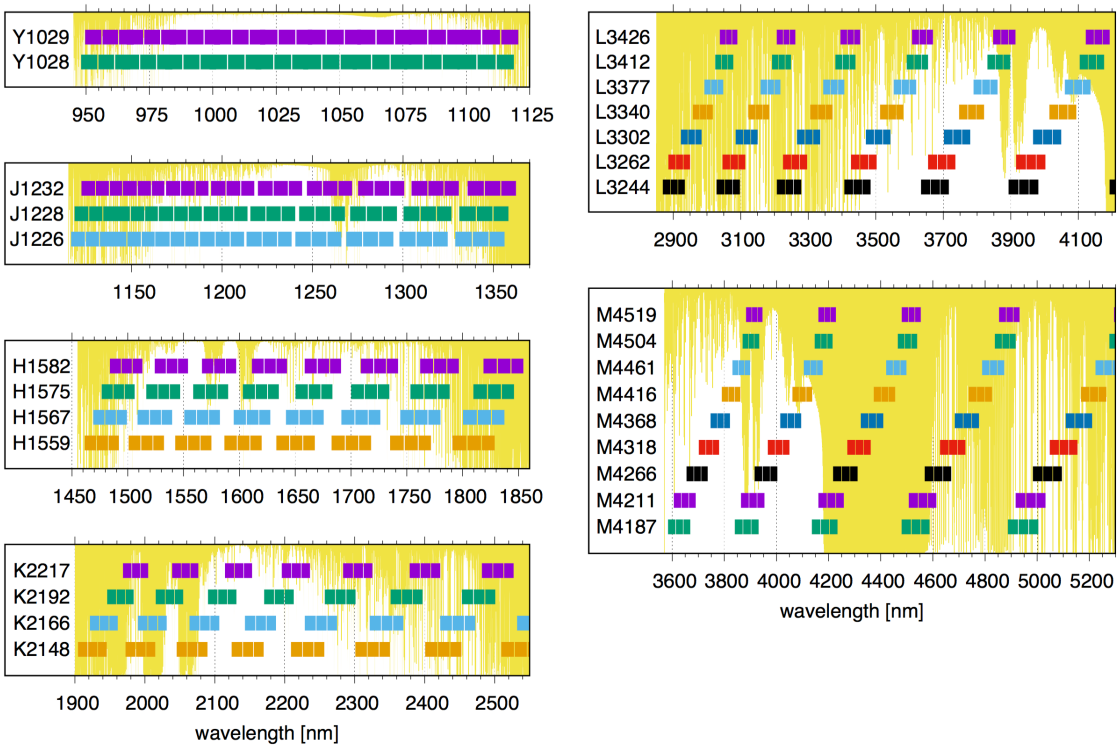

Figure 2.3: *CRIRES+ wavelength settings compared to the atmospheric transmission. In this work the K2166 and H1582 configurations were used.*

2.3 The Liller 1 dataset

The CRIRES+ data of the analysed sample have been acquired over the last year (between April 2023 and July 2024) under favourable sky conditions of clearness and seeing. Each star has been observed through the H1582 and K2166 gratings.

After the standard dark and flat-field corrections, each spectrum was sky subtracted by using nod pairs. The nodding is a classical technique specifically adopted to optimally subtract the background and other instrument effects. It consists in observing a given target at two positions along the slit (named A and B), with the specific purpose of removing the sky emission lines. The target is alternatively centered on position A and B along the slit. The separation between the A and B positions (*nodding throw*) has to be set by the observer in order to avoid contamination by nearby stars, but it cannot exceed the slit length of 10". The sky background is

effectively removed by subtracting one frame from the other and vice versa. This process is sometimes called *double subtraction*. The total on source integration time is split in N pairs of sub-exposures, where N is the requested number of AB nodding cycles. The combined spectrum contains the summed counts of A and B.
Then, every spectrum was calibrated in wavelength using arc lamps and extracted using the optimal extraction method, a procedure that minimises the loss of spectral resolution, maximises the signal-to-noise ratio, and efficiently identifies local outliers. Optimal extraction is a key step in processing the raw images of spectra as registered by two-dimensional detector arrays to a one-dimensional format. The signal-to-noise ratio of the final 1D spectra is always $\geq$40.

ID	Ra [deg]	Dec [deg]	J [mag]	K [mag]
100437	263.3524868	-33.3922546	13.946	11.637
100760	263.3501594	-33.3993386	14.899	12.485
100964	263.3561862	-33.3905949	14.864	12.418
300553	263.3497432	-33.3890865	14.313	11.774
300614	263.3457652	-33.3873565	14.775	12.454
300682	263.3497083	-33.3888985	14.721	12.460
300727	263.3449122	-33.3858666	14.913	12.496
400778	263.3544150	-33.3881915	15.070	12.862
400829	263.3516455	-33.3882126	15.057	12.801
400887	263.3538377	-33.3873272	15.194	12.927

Table 2.2: *Liller 1 analysed targets characteristics.*

The observed sample includes a total of ten stars members of Liller 1, sufficiently bright to be observed at high spectral resolution in the H and K band with CRIRES+. The selected stars are luminous giants, $\sim$2 - 2.5 magnitudes brighter than the red clump, chosen from the NIR colour-magnitude diagram (CMD). All of them are located in the central region, within r $\leq$ 35" from the cluster centre (Figure 2.4). All the observations have been planned with the 0.4" wide slit, thus providing an overall spectral resolution R $\sim$ 50,000.
The membership of every star to Liller 1 is further tested observing proper motions (PMs), combining high-resolution HST and adaptive optics assisted GeMS/GEMINI images of the central region of the cluster, secured over a time baseline of 6.3 years (Ferraro et al. 2021b, Dalessandro et al. 2022b). Nine of the ten spectroscopic targets are located within 0.7 $mas\ yr^{-1}$, corresponding to three times the average PM error in that magnitude bin, as expected for likely cluster members. The remaining

target (namely, 300553) lies exactly in the gaps of the GeMS detector, and no PM can be measured for it. At the same time, it is located at only 8" from the center of Liller 1, and consequently Gaia PM measurements (Gaia Collaboration et al. 2016, 2023) are not available for this object. Despite everything, its position in the CMD (lying at K $\sim$ 11.8 and J-K $\sim$ 2.5, just along the red giant branch, see Figure 2.4), its central position (where member stars are largely dominant with respect to field interlopers), and its measured radial velocity (Table 4.1) confirm that it is also a high-probability cluster member.
Table 2.2 lists coordinates and magnitudes corrected for differential reddening (from Valenti et al. 2010, Ferraro et al. 2021b) of the ten targets.

Both the H and the K bands are optimal for the chemical study of heavily reddened stars, as they contain numerous atomic lines of iron and α-elements, which are highly effective tracers of the enrichment timescale of a stellar population. More specifically, the H band is an infrared region centered at a wavelength of 1.65 μm, situated in a clear window between atmospheric absorption bands. In the majority of red giant stars, the most prominent spectral features in the H band are a series of absorption bands attributed to the CO and OH molecules, from which accurate abundances of carbon and oxygen can be derived. The K band, instead, represents another atmospheric window within the near-infrared range, centered at a wavelength of 2.2 μm. Of particular significance is the 2.0-2.4 μm spectral region, which encompasses numerous useful molecular vibration-rotation transitions from CO, HF, H_2O and CN. These elements provide essential insights into the chemical mixing processes of cool stellar atmospheres in the Post Main Sequence evolutionary phase. Furthermore, for Liller 1, dust extinction is approximately 14 mag in the V band, 4.0 mag in the J band, 2.5 mag in the H band and 1.6 mag in the K band. Consequently, high-resolution spectroscopy in the H and K bands is the best method for studying the chemistry of this stellar system.

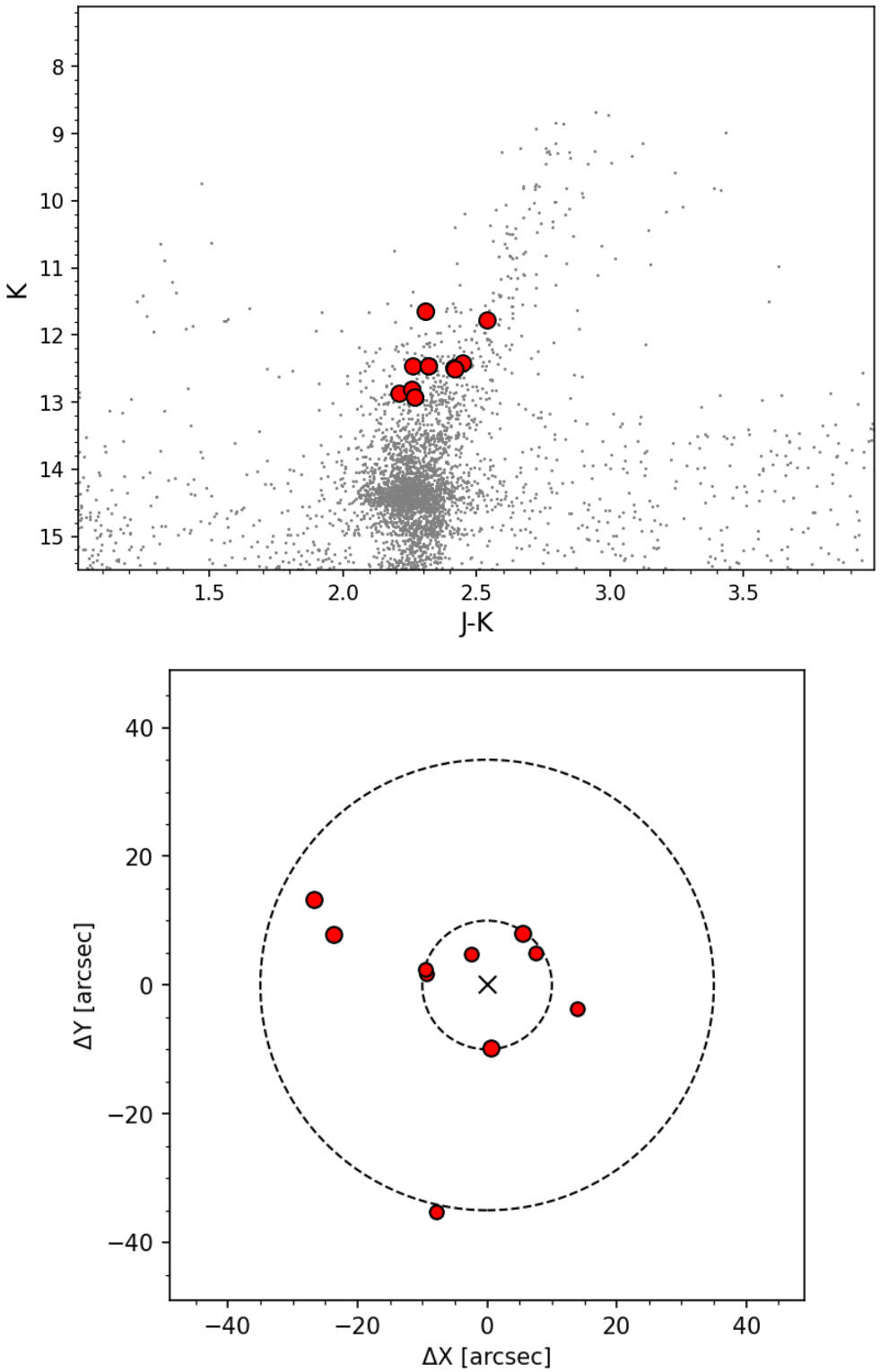

Figure 2.4: *Top panel: Liller 1 K, J-K CMD (grey dots) with highlighted the analysed stars (red circles), observed with CRIRES+.*
Bottom panel: Position of these spectroscopic targets in the plane of the sky with respect to the cluster centre, which is marked with a cross ($RA_0 = 263.3523333$, $Dec_0 = -33.3895556$).
The dashed circles mark the distance at 10″ and 35″ from the centre.

Chapter 3

Spectral Analysis

A generic stellar spectrum is composed of a continuum and a number of distinct absorption features. The continuum encompasses a broad spectrum of wavelengths and is the result of black body emission. In contrast, the spectral lines are caused by atomic and molecular absorption processes within the stellar atmosphere, and are at specific wavelengths depending on the transition. The shape of the lines could be in first approximation reproduced by a Gaussian function. The position and intensity of the absorption provide us with crucial information about certain stellar characteristics, such as radial velocity and chemical composition.
The analysed observed spectra are the convolution of the source spectral energy distribution (SED) with the instrumental response of the spectrograph. In order to obtain the correct information from these spectra it is therefore first necessary to implement some corrections, which will be described in detail in the following sections.

3.1 Normalization and telluric correction

Before a correct continuum normalization is achieved, a preliminary step is applied, which consists in the rebinning of the spectrum to increase the signal-to-noise ratio (SNR). The latter quantity is calculated before and after the rebinning operation to verify the result.
Subsequently, the observed spectrum may be globally normalised by working on each order and chip. Every order comprises three chips, with six orders for the

K-band and seven for the H-band. In general, the normalization process is divided into a global normalization, where the continuum can be fitted via smoothing or via polynomial/spline fitting, and into a subsequent local normalization in which a correction factor is applied to refine the continuum around each line of interest.
In order to rectify and globally normalize the CRIRES+ spectra a smoothing low-pass filtering is applied, which consists of taking the median value for every small spectral region, typically comprising a few hundred pixels, in order to construct the continuum. Subsequently, the spectrum is divided by the continuum obtained. The "local" normalization consists instead of small corrections applied to each line during the chemical analysis.
This step is crucial as the chemical abundances are strongly dependent on the position of the continuum and a possible uncertainty in the calculation of the latter can result in significant alterations of the derived abundance. In particular, the analysed star sample comprises cool stars, which are characterized by spectra that are densely populated by metallic lines and molecular bands. This increases the complexity of the definition of the continuum and the normalization process. Therefore, high resolution is essential to better locate the continuum and obtain more precise results.
An example of a CRIRES+ spectrum before and after the rebinning and the normalization is presented in Figure 3.1 and 3.2, respectively.

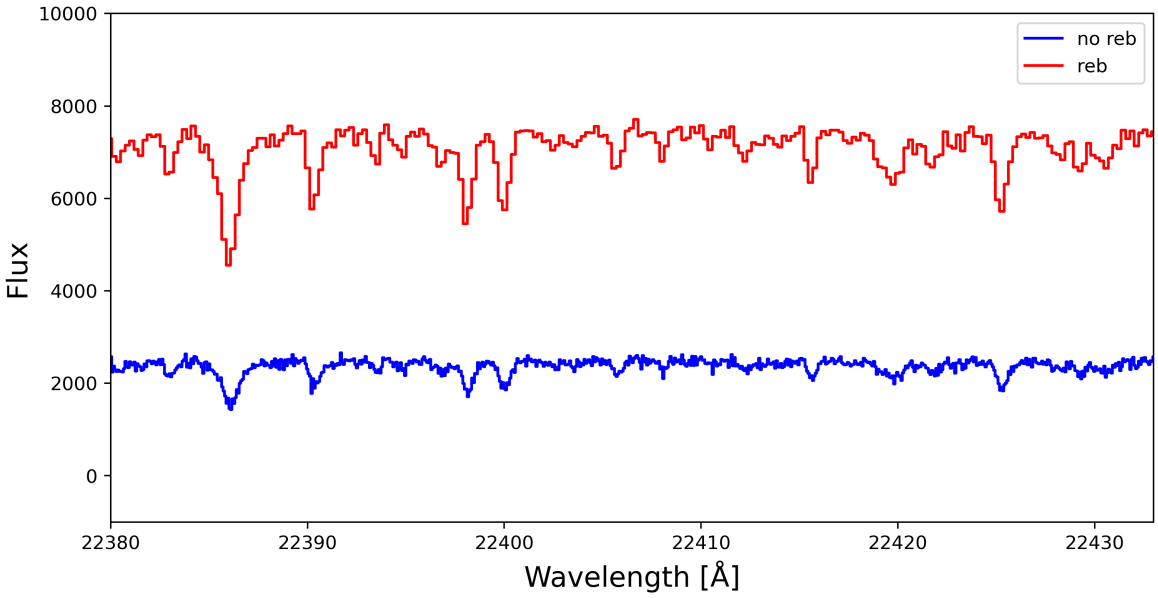

Figure 3.1: *Comparison of the original spectrum (blue line) to the rebinned one (red line) for star ID400887.*

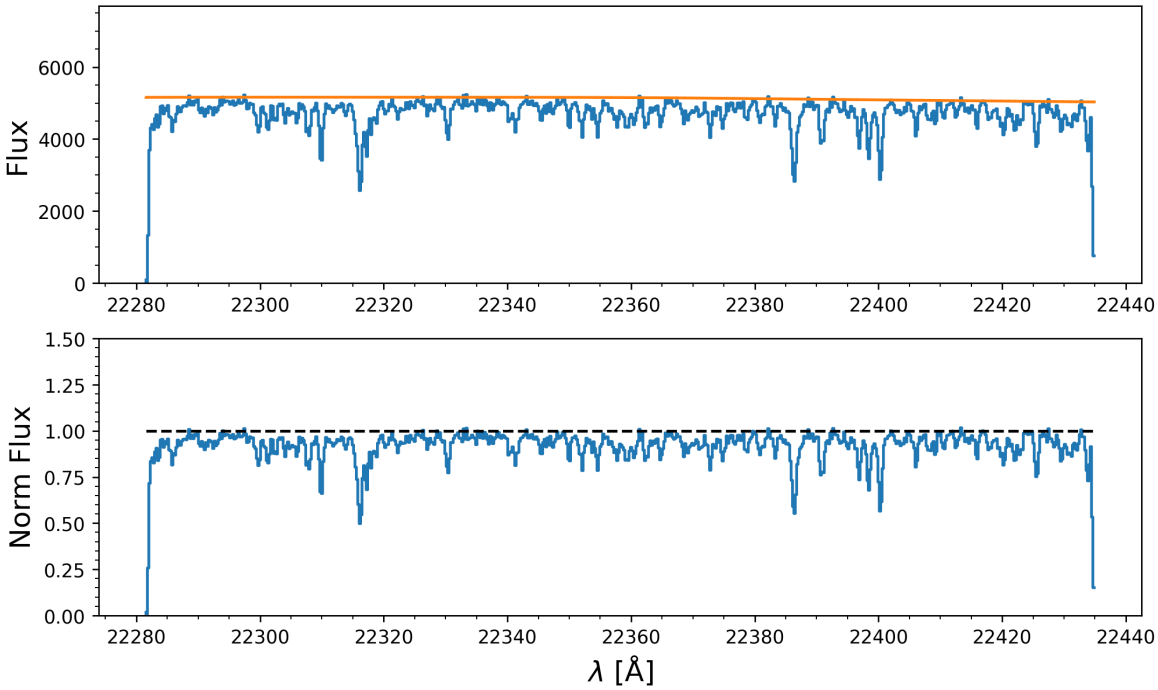

Figure 3.2: *Global normalization of one chip of the K-band spectrum of the ID300727 star. The observed spectrum and the continuum are reported in blue and in orange, respectively.*

The final required preliminary correction is the removal from the observed spectrum of the telluric (earth originated) lines, namely the telluric correction. In fact, when utilising a ground-based telescope, the light passes through the atmosphere and interacts with atoms and molecules resulting in the formation of absorption features that contaminate the observed spectrum. Specifically, the infrared region exhibits a multitude of transitions observed in various molecules, including H_2O, O_2, CO_2, CH_4.

However an appropriate telluric spectra can be constructed from the TAPAS portal, at the required spectral resolution (in our case R=50,000) inserting the observing date, site (in our case Cerro Paranal in Chile) and precipitable water vapour. The telluric correction is then performed by dividing the normalized spectrum to the normalized telluric spectrum.

In the following radial velocity and chemical abundance analysis, it is preferable to avoid regions that were particularly affected by telluric lines, as the correction may not be optimal in such regions, and residuals could contaminate the spectrum.

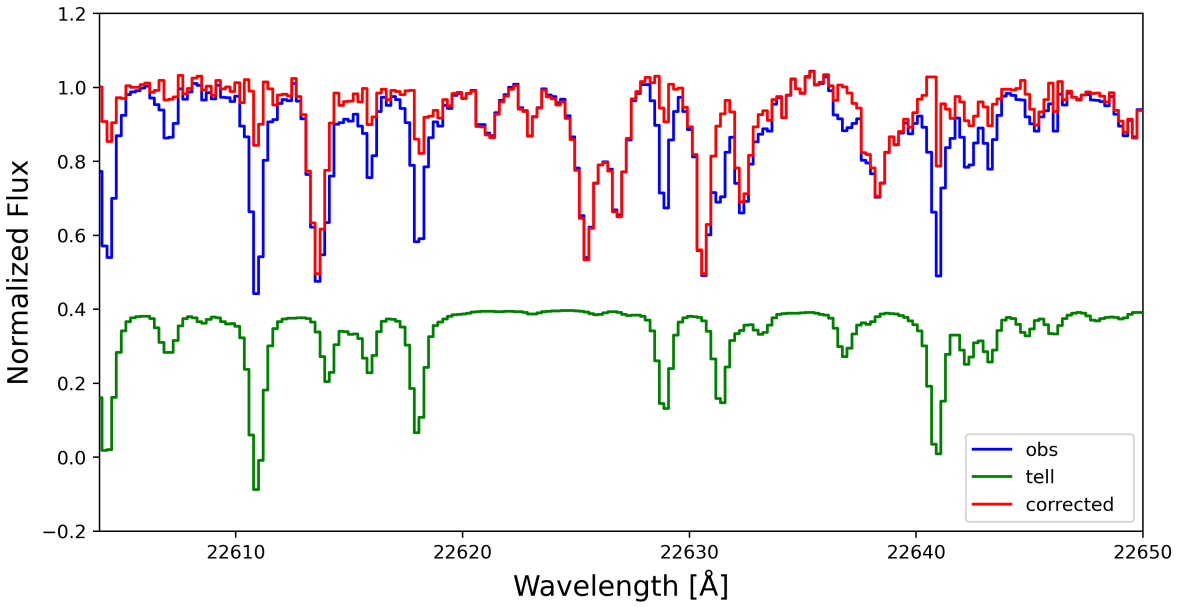

Figure 3.3: *Telluric correction applied to one chip of the K-band spectrum of the ID300727 star. The blue spectrum is the observed one, while the telluric spectrum is shown in green. The final result is reported in red.*

3.2 Radial velocity correction

The radial velocity of a star is defined as its velocity with respect to the observer along the line of sight. This kind of motion produces the so-called Doppler effect, which consists of a shift in the position of spectral lines at different frequencies. In particular, a star exhibiting a blue-shift is moving towards the observer, while a star exhibiting a red-shift is moving away from the observer.

In order to obtain this essential information, the cross-correlation function (Lockwood et al. 2014) between the observed spectrum and a synthetic spectrum has been computed. For each star in the sample, a synthetic spectrum constructed with a zero velocity and similar stellar parameters (temperature [T] and gravity [log(g)]) was employed. This one is shifted pixel by pixel along the observed spectrum, which instead remains fixed, to maximize the correlation probability. Then the observed spectrum is corrected of the right amount (see Fig. 3.4). In order to optimize the result, the spectrum region selected for this procedure must be devoid of telluric lines and possess discernible features. In the K-band, the 22290-22410 Å range has been chosen, whereas in the H-band the focus is on the 15247-15311 Å region.

The spectrum is also affected by a Doppler-shift due to the Earth's motion around the Sun, so the value of the radial velocity obtained from the procedure must be

corrected for this effect. The so-called heliocentric correction must be applied, taking into account the date of the observations, the coordinates of the source and the coordinates of the observatory. The final corrected radial velocities for the 10 stars discussed here are reported in Table 4.1.

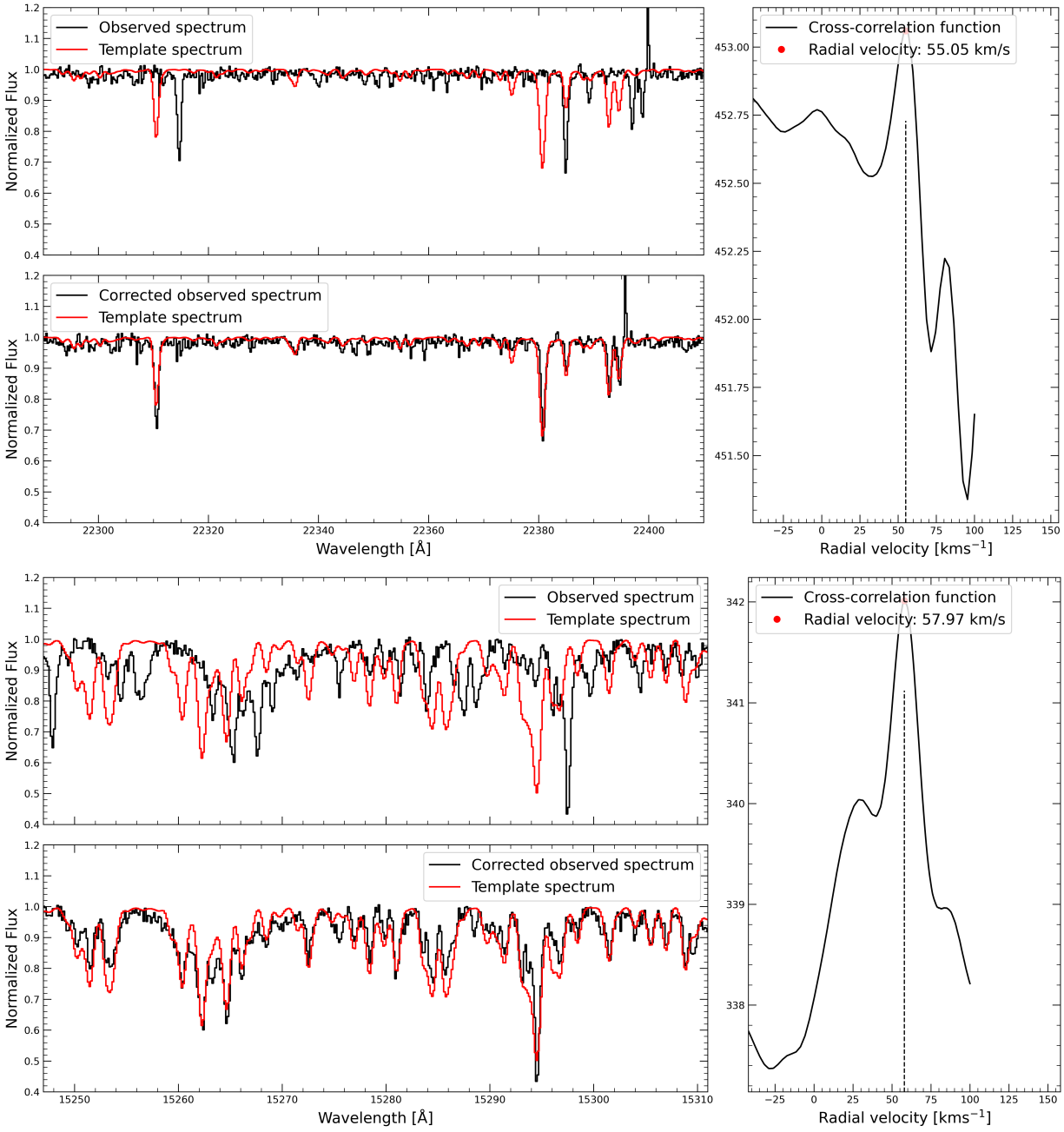

Figure 3.4: *Radial velocity correction of the ID100964 star in the K-band (up) and in the H-band (down). For every image, in the upper left the synthetic spectrum (red) and the not corrected observed spectrum (black) are reported, while in the lower left the corrected spectrum is shown. On the right, the cross-correlation function can be observed.*

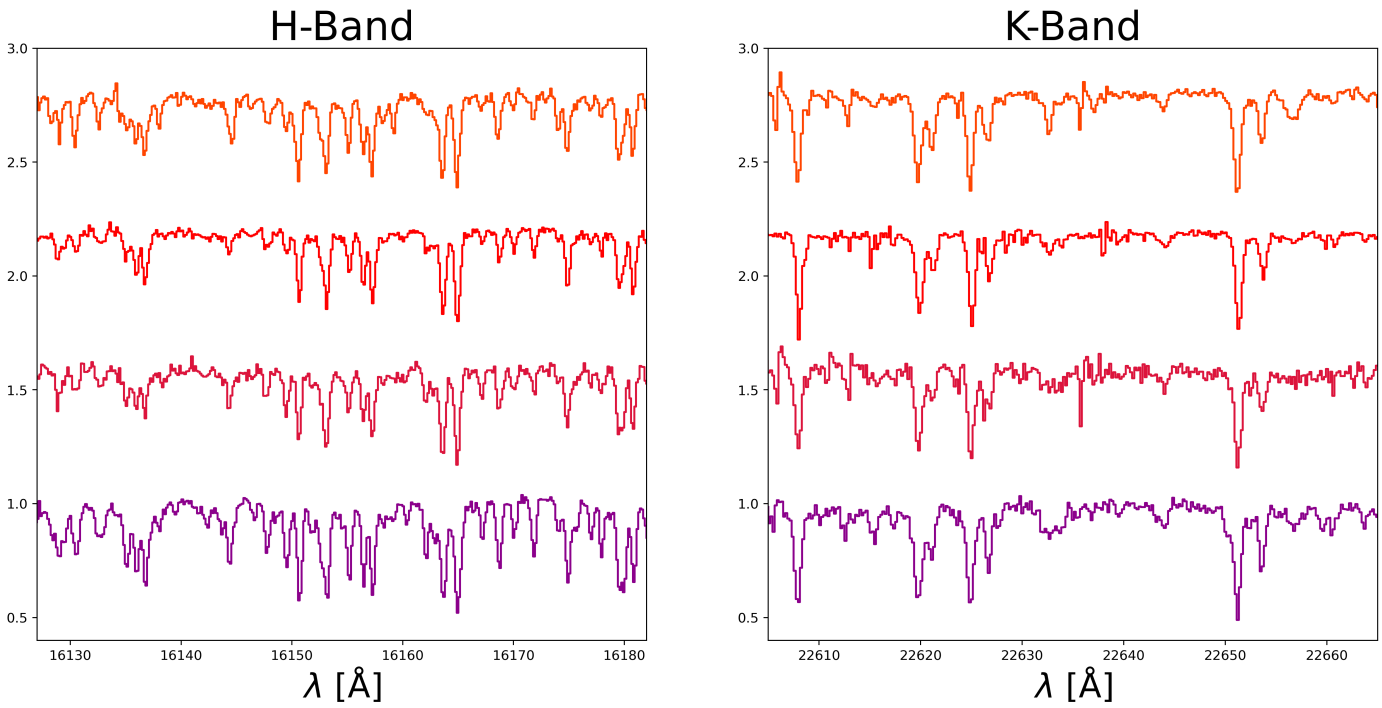

Figure 3.5: *Normalized and completely corrected CRIRES+ spectra in two significant region, respectively of the H and the K band, of four representative Liller 1 giant stars with different temperatures.*
From the top: $T_e = 4050\ K$, $T_e = 4150\ K$, $T_e = 4200\ K$, $T_e = 4300\ K$.

3.3 Observed spectral resolution

Before starting the chemical analysis, it is essential to identify the observed spectral resolution of the spectra, as this is a prerequisite for the preparation of the synthetic spectra that will be employed (see next section). It is important to note that the width of the spectral lines, in terms of wavelength, is not infinitesimal. The broadening (the full width at half maximum, FWHM) in the observed spectrum is the convolution of several effects:

- Intrinsic broadening
- Instrumental broadening
- Rotation/Convection

Intrinsic profile

As already mentioned, spectral lines are not strictly monochromatic, but intrinsically show a broadening due to different physical phenomena. The first, from a theoretical

point of view, is the natural broadening given by the Heisenberg's principle, one of the basic tenets of quantum mechanics. The principle states that, in a physical phenomenon, the product of uncertainties ΔE and Δt takes the minimum value:

$$\Delta E \cdot \Delta t \sim \frac{h}{2\pi}.$$

Knowing that the average lifetime of excited atomic states is finite, this implies that $\Delta E \neq 0$, indicating that the frequency of the emitted photon is also subject to inherent uncertainty. Another possible effect is the pressure, or collisional, broadening, which arises from collisions between excited atoms and is particularly significant at high pressures. Both effects are present, but their contribution to the final broadening is minimal.

The main intrinsic profile is determined by the thermal motions of atoms and molecules in the photospheric gas, a phenomenon known as thermal broadening. Under the condition of local thermal equilibrium, the velocities of atoms and molecules follow a Maxwell-Boltzmann distribution with a dispersion

$$\Delta v_{th} = \sqrt{\frac{2kT}{m}},$$

where k is the Boltzmann constant, m is the mass of the absorbing particles and T is their temperature. As the temperature of the gas increases, the atoms will exhibit greater velocity and, consequently, broader lines. Typically in cool stars the thermal broadening is $\leq 1 - 2$ Km/s. At these temperatures (around 4,000 K), such term is insufficient for reproducing the line core width and therefore it is necessary to add in quadrature an additional velocity component, named microturbulence. This broadening is typically around 2 km/s for giant stars. The conventional method for calculating microturbulence is to search for the value that minimizes trends between the iron abundance [Fe/H] and the reduced equivalent width $log_{10}(EW/\lambda)$.

Instrumental profile

The instrumental profile is determined by the spectral resolution of the used spectrograph, which is set in this specific case by the slit width. It is a measure of the capability of the instrument to resolve spectral features and it is defined by the following formula:

$$R = \frac{\lambda}{\Delta\lambda} = \frac{c}{\Delta v} \tag{3.1}$$

where $\Delta\lambda$ is the FWHM and represents the minimum wavelength separation between two resolved features in the electromagnetic spectrum. Higher resolution allows for the distinction of a greater number of lines in the spectrum, resulting in a larger statistical sample. When the resolution is fixed, the FWHM increases with the wavelength. In most cases, instrumental broadening is the dominant factor, but increasing the instrumental resolution, the FWHM decreases and other effects can be appreciated, especially the broadening arising from velocity fields. For CRIRES+ spectra the resolving power is fixed at $R \sim 50,000$ (FWHM $\sim$ 6 km/s).

Rotation/Convection effect

The final significant processes that may impact the profile of spectral lines are the possible stellar rotational velocity and the velocity fields within stellar atmospheres, i.e. convection. This broadening is primarily discernible at high resolution, as previously outlined. In particular, the observed spectra of giant stars appear broader than the expected resolution of the echelle spectrograph, and this is ascribed to turbulent motions of the gas cells, whose size is greater than the mean free path of a photon. Red giants, in fact, are characterized by an important external convective region, due to their proximity to the Hayashi track. This additional velocity component is named macroturbulence and it is typically ≥ 10.

Ultimately the measured FWHM is the sum in quadrature of the broadening given by the different effects:

$$FWHM_{obs} = \sqrt{(FWHM_{instr})^2 + (FWHM_{intrinsic})^2 + (FWHM_{rot/conv})^2} \quad (3.2)$$

To optimally match the observed spectra, each synthetic spectrum, which is normally computed at the nominal spectrograph resolution, must be convolved with a Gaussian profile that reproduces the additional broadening (macroturbulence).

3.4 Chemical analysis

As quoted above, the measure of the chemical abundances has been performed via the spectral synthesis technique, which is a method widely adopted in the literature. The method consists in comparing the observed spectrum with a grid of suitable synthetic spectra with specified temperature and gravity but with different

abundances. The best fit models will be able to reproduce all the absorption lines identified in the observed spectrum.

The construction of the model requires two principal elements: the model atmosphere and the atomic and molecular data, which, in this case, must include all the existing lines in the NIR. In particular, the model atmosphere provides the evolution of the most important thermodynamic quantities (temperature, pressure etc.) as a function of optical depth, and describes the continuum of the spectrum. Furthermore, the strength of a line is closely related to the population of the atomic levels involved in the transition, which in turn depends on parameters such as temperature and gravity.

Going in detail, the synthetic spectra exploited in our analysis have been generated using the radiative transfer code Turbospectrum (Alvarez & Plez 1998; Plez 2012; de Laverny et al. 2012), under the Local Thermal Equilibrium (LTE) approximation, the MARCS models atmospheres (Gustafsson et al. 2008), the atomic data from VALD3[1] (Ryabchikova & Pakhomov 2015) and the most updated molecular data from B. Plez website[2].

For both H and K bands we have two sets of synthetic spectra, one solar-scaled and one with some enhancement of [α/Fe] abundance (i.e. +0.3 dex). In both grids, the spectra have a temperature range between 3000 and 5000 K with 50 K steps, and a log(g) range between 0.0 and 3.5 with an increment of 0.25. For fixed stellar parameters, spectra have an iron abundance [Fe/H] ranging from -1.0 to 0.5 dex, with a step of 0.25 dex, that is the wide range spanned by the Liller 1 stellar populations. Finally, every spectrum shows a nitrogen enhancement ([N/Fe] = 0.5 dex) and a carbon depletion ([C/Fe] = -0.3 dex), linked to the presence of convection on the surface of RGB stars.

The temperature and gravity of every observed star have been obtained photometrically by projecting each of them on an isochrone that reasonably matches the observed CMD. An isochrone is an ideal curve on the theoretical temperature-luminosity plane (Hertzsprung-Russell diagram) or, equivalently, on the observational color-magnitude plane, representing a population of stars with different masses at the same age. The used sample of isochrones comes from the set of Bressan et al. (2012).

[1] http://vald.astro.uu.se/
[2] https://www.lupm.in2p3.fr/users/plez/

Element	Wavelength [Å]	E.P. [eV]	log(gf)
Fe I	15013.771	6.22	0.087
Fe I	15239.712	6.42	-0.032
Fe I	15301.558	5.92	-0.687
Fe I	15343.788	5.65	-0.582
Fe I	15671.004	6.33	-0.221
Fe I	15741.917	5.65	-0.100
Fe I	15821.712	5.64	-0.792
Fe I	15911.302	5.87	0.104
Fe I	15934.018	6.31	-0.290
Fe I	16125.898	6.35	0.860
Fe I	16156.557	5.96	-0.290
Fe I	16171.930	6.38	-0.450
Fe I	16177.990	6.38	-0.402
Fe I	16180.899	6.28	0.295
Fe I	16292.840	5.92	-0.157
Fe I	16331.523	5.98	-0.392
Fe I	17161.104	6.02	-0.070
Fe I	17282.291	6.43	0.097
Fe I	17695.936	5.95	-0.517
Fe I	17706.615	6.58	0.605
Mg I	14898.691	6.72	-1.640
Mg I	17749.615	6.73	-1.495
Si I	15243.588	6.73	-0.867
Si I	15361.161	5.95	-2.080
Si I	15827.213	7.09	-0.654
Si I	15833.603	6.22	-0.187
Si I	16129.016	7.14	-0.659
Si I	16163.691	5.95	-0.860
S I	15469.816	8.05	-0.050
S I	15478.482	8.05	0.180
Ca I	16136.823	4.53	-0.363
Ca I	16150.763	4.53	-0.032
Ca I	16155.236	4.53	-0.500
Ca I	16157.360	4.55	0.246
Ti I	15315.585	2.34	-2.080
Ti I	16330.532	3.11	-0.890
Ti I	16635.160	2.34	-1.580
Ti I	17376.576	4.49	0.750

Table 3.1: *H-band line list.*

Element	Wavelength [Å]	E.P. [eV]	log(gf)
Fe I	21553.299	6.70	-0.500
Fe I	21735.457	6.18	-0.715
Fe I	21813.977	5.85	-1.390
Fe I	21832.980	6.78	-2.166
Fe I	21851.381	3.64	-3.610
Fe I	22380.797	5.03	-0.460
Fe I	22385.102	5.32	-1.350
Fe I	22392.879	5.10	-1.250
Fe I	22419.977	6.22	-0.150
Fe I	22473.264	6.12	0.440
Fe I	22493.672	5.83	-0.890
Fe I	22619.838	4.99	-0.360
Mg I	21458.863	6.52	-1.320
Mg I	21536.220	6.78	-1.860
Mg I	21761.020	6.98	-0.560
Mg I	23328.094	6.72	-1.490
Si I	21754.434	7.30	-0.670
Si I	21779.660	6.72	0.420
Si I	21837.953	7.07	-0.889
Si I	22537.533	6.62	-0.230
Si I	22665.758	6.62	-0.680
S I	22507.357	7.87	-0.480
S I	22644.057	7.87	-0.340
S I	22707.738	7.87	0.440
Ca I	22607.943	4.68	0.520
Ca I	22624.963	4.68	0.687
Ca I	22626.723	4.68	-0.220
Ca I	22651.178	4.68	0.850
Ca I	22653.578	4.68	-0.220
Ti I	21532.820	3.90	-0.700
Ti I	21782.943	1.75	-1.170
Ti I	22310.617	1.73	-2.070
Ti I	22443.926	1.74	-2.360
Ti I	22621.221	1.75	-2.740
Ti I	22632.742	1.88	-2.760
Sc I	21812.055	1.43	-1.958
Sc I	22394.670	1.43	-1.196
V I	21563.950	2.51	-0.620

Table 3.2: *K-band line list.*

Knowing the possible presence of multi-iron and multi-age sub-population in Liller 1, an iterative process has been adopted. Initially, it is assumed that all stars belong to the main, old population, which exhibits a sub-solar metallicity. The stellar parameters are thus calculated by projecting the stars over an isochrone of 12 Gyr and with a metallicity [Fe/H] = -0.3 dex. Obtained the temperature and gravity values for each star, a first measurement of the chemical abundances is carried out, with a particular focus on the iron abundance. If some stars show a significantly more metal-rich abundance with respect to the old population, their stellar parameters should be recalculated. These stars are re-projected onto a new isochrone better describing the young solar-scaled sub-population of Liller 1, which is estimated to be approximately 2 Gyr old and has a metallicity of +0.3 dex. Subsequently, the chemical analysis is repeated considering the right temperature and gravity. Nevertheless, it is important to mention that the impact of the chosen isochrone on the determination of the stellar parameters affect essentially only the gravity, with an overall impact on the derived abundances of less than 0.1 dex. In the final analysis, temperatures in the range of 3900 - 4300 K (with uncertainties of $\pm$ 100 K), and surface gravities in the range of log(g) = 1.25 - 2.00 (with a $\pm$ 0.3 uncertainty) have been estimated.

The spectral synthesis technique consists in comparing observed and synthetic spectra using specific statistical tools, such as the minimization of the χ^2 distribution, and/or the line strength. In this Thesis, the analysis has been carried out around selected individual lines by using as a figure of merit their strength, which depends on both their excitation potential and their transition probability. Therefore, an appropriate list of spectral lines has to be defined and optimized, according to the spectral range, stellar properties and spectral resolution of the observed spectra, both for the H and K bands (Tables 3.1 and 3.2). The selection of lines is mainly based on the existing literature (Afşar et al. 2018; Fanelli et al. 2021,2022; Lim et al. 2022), with the addition of a few isolated lines, selected from the VALD3, NIST[3], and Kurucz[4] databases. These safely measurable lines are first visually inspected in both synthetic and observed spectra. Naturally, the selected lines have to be poorly contaminated by nearby lines or strong telluric lines and must not be saturated, in order to maximise the accuracy of the chemical analysis.

[3] https://www.nist.gov/pml/atomic-spectra-database
[4] http://kurucz.harvard.edu/

For each star, an input file has been compiled, containing the following information for every line:

- the line wavelength in Angstrom,
- the local normalization factor, to refine the continuum level,
- the local velocity shift, to perfect the radial velocity correction,
- the number of pixels to be used to calculate the line strength (usually pixel=3),
- its excitation potential E.P. and its transition probability log(gf).

This input file is read by a Python script to perform the spectral synthesis which is described below.
For each spectral feature, the line strength has been computed by integrating the line flux within its core profile, avoiding the line wings which may be more contaminated by small nearby lines. The selected lines are measured in the observed spectrum as well as in all the synthetic spectra with different abundances in steps of 0.25 dex.
Afterwards, a pseudo curve-of-growth is built up by interpolating the measurements obtained from the set of synthetic spectra. The element abundances are shown on the x-axis, while the line strengths are shown on the y-axis. To finally obtain the chemical abundance, the observed line strength is interpolated with the curve-of-growth, as shown in Figure 3.6.
The accuracy of the measured chemical abundances depends on both the quality of the synthetic spectra and the quality of the observed spectra, and therefore on the applied normalization and corrections.

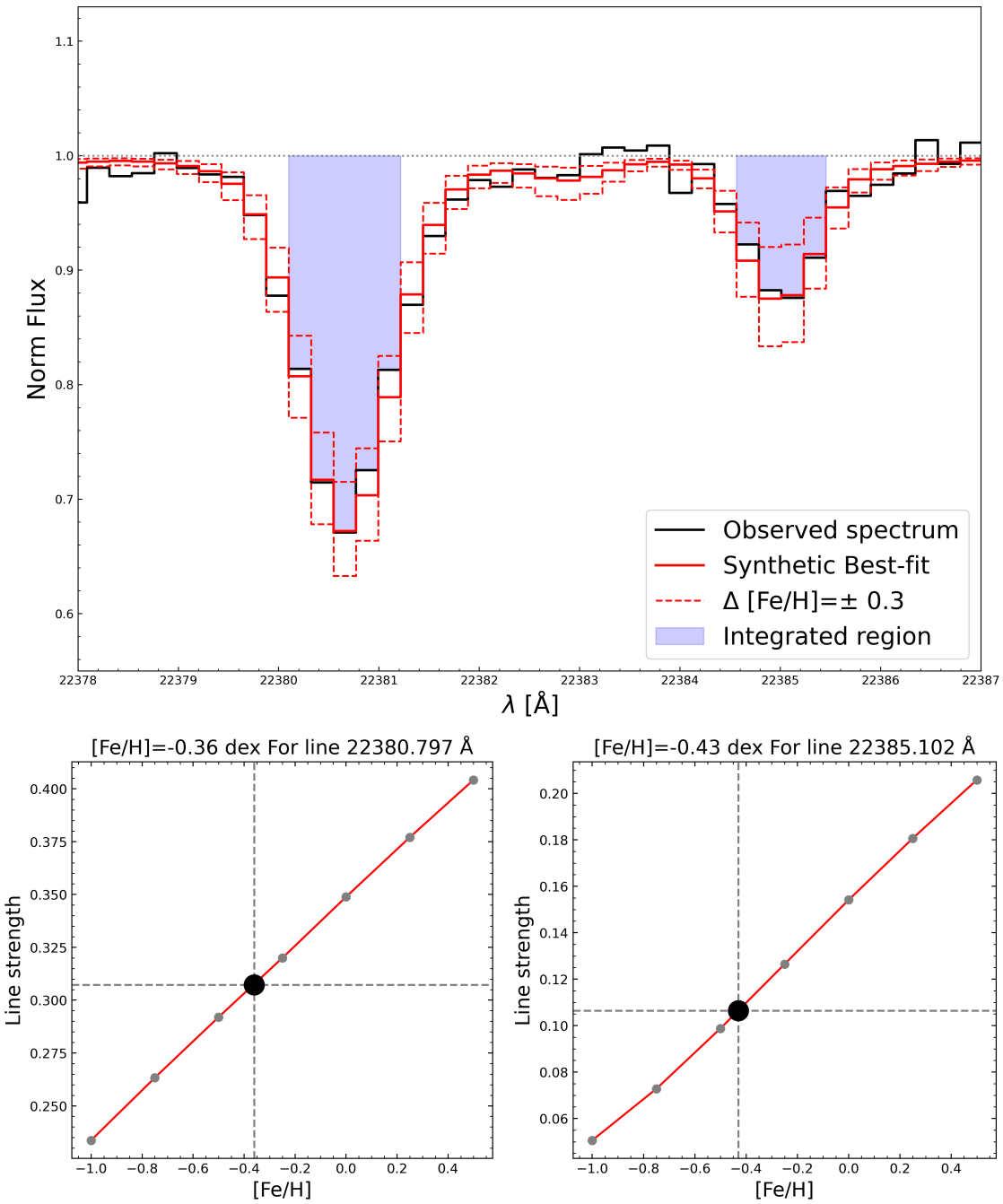

Figure 3.6: *Line strength measurement of the Fe I lines at 22380.797 Å and 22385.102 Å in the K-band. Top panel: spectral synthesis technique employed to measure the chemical abundance of the most significant elements. The observed spectrum is represented by the black line, while the best-fit synthetic spectrum is shown in red. The integrated region (blue area) and two other spectra with a deviation of ±0.3 dex from the best-fit (dashed red lines) are also presented. The shaded blue areas indicate the core regions where the line strengths have been computed. Lower panels: pseudo-curve-of-growths (red lines) constructed for the two iron lines by interpolating the line strength measurements in the set of synthetic spectra with the same stellar parameters as the observed star spectrum and varying element abundance within the selected range between -1.0 and +0.5 dex, with a step size of 0.25 dex (grey dots). The position in which the measured line strength of the observed spectra intersects the pseudo-curve-of-growth is indicated by a black larger dot.*

Chapter 4

Results and conclusions

The physical and chemical characteristics of the ten stars of Liller 1 analysed in this work are presented in Table 4.1. In particular, the temperature, gravity, radial velocity, iron abundance, α-elements abundance (specifically, [Mg/Fe], [Si/Fe], [S/Fe], [Ca/Fe], and [Ti/Fe]) and iron-peak elements abundance ([Sc/Fe] and [V/Fe]) are reported for each star.

ID	T [K]	log(g)	RV [km/s]
100437	3950	1.50	72.2
100760	4200	1.50	68.6
100964	4150	1.50	56.0
300553	4050	1.25	68.4
300614	4150	1.75	74.7
300682	4150	1.50	73.6
300727	4200	1.75	71.6
400778	4300	1.75	71.6
400829	4250	1.75	64.2
400887	4300	2.00	70.8

ID	[Fe/H] dex	[Mg/Fe] dex	[Si/Fe] dex	[S/Fe] dex	[Ca/Fe] dex	[Ti/Fe] dex	[Sc/Fe] dex	[V/Fe] dex
100437	0.01±0.02	0.08±0.02	0.10±0.02	0.18±0.02	0.01±0.02	-0.10±0.10	-	-
100760	-0.58±0.01	0.36±0.01	0.37±0.01	0.49±0.01	0.26±0.04	0.24±0.02	0.16±0.01	0.19±0.10
100964	-0.57±0.01	0.37±0.01	0.27±0.01	0.27±0.10	0.21±0.03	0.29±0.01	0.09±0.10	-0.04±0.10
300553	-0.56±0.02	0.37±0.03	0.24±0.02	0.39±0.02	0.29±0.04	0.39±0.02	-	0.13±0.10
300614	0.18±0.01	0.02±0.02	0.04±0.01	0.05±0.01	-0.07±0.01	-0.05±0.01	-0.11±0.02	-0.23±0.10
300682	-0.37±0.01	0.36±0.01	0.33±0.01	0.35±0.01	0.30±0.01	0.39±0.01	0.28±0.10	0.15±0.10
300727	0.19±0.01	-0.07±0.01	0.02±0.02	0.00±0.04	0.08±0.01	0.08±0.01	-	0.10±0.10
400778	-0.16±0.02	0.28±0.02	0.26±0.02	0.26±0.02	0.24±0.02	0.14±0.02	0.14±0.02	0.13±0.10
400829	-0.44±0.01	0.36±0.01	0.29±0.01	0.21±0.03	0.38±0.01	0.34±0.02	0.18±0.01	0.27±0.10
400887	0.20±0.01	-0.02±0.02	0.01±0.02	0.04±0.02	0.03±0.01	0.03±0.01	0.01±0.03	-0.04±0.10

Table 4.1: Stellar parameters, radial velocity and abundances with corresponding errors of every star of the Liller 1 data sample.

4.1 Kinematics

The observed stars have been selected on the basis of their proper motions. However radial velocities provide a further important confirmation of the membership of the observed sample to Liller 1, since proper motions of the system partially overlap those of the bulge field. Moreover they complete the 3D kinematics information, providing a comprehensive three-dimensional velocity map of the multi-iron content which is essential to future explorations of the global kinematics of the multi-iron sub-populations.

The radial velocities of the analysed stars have been determined through the application of cross-correlation techniques between the observed and the synthetic spectra, as explained in Section 3.2.

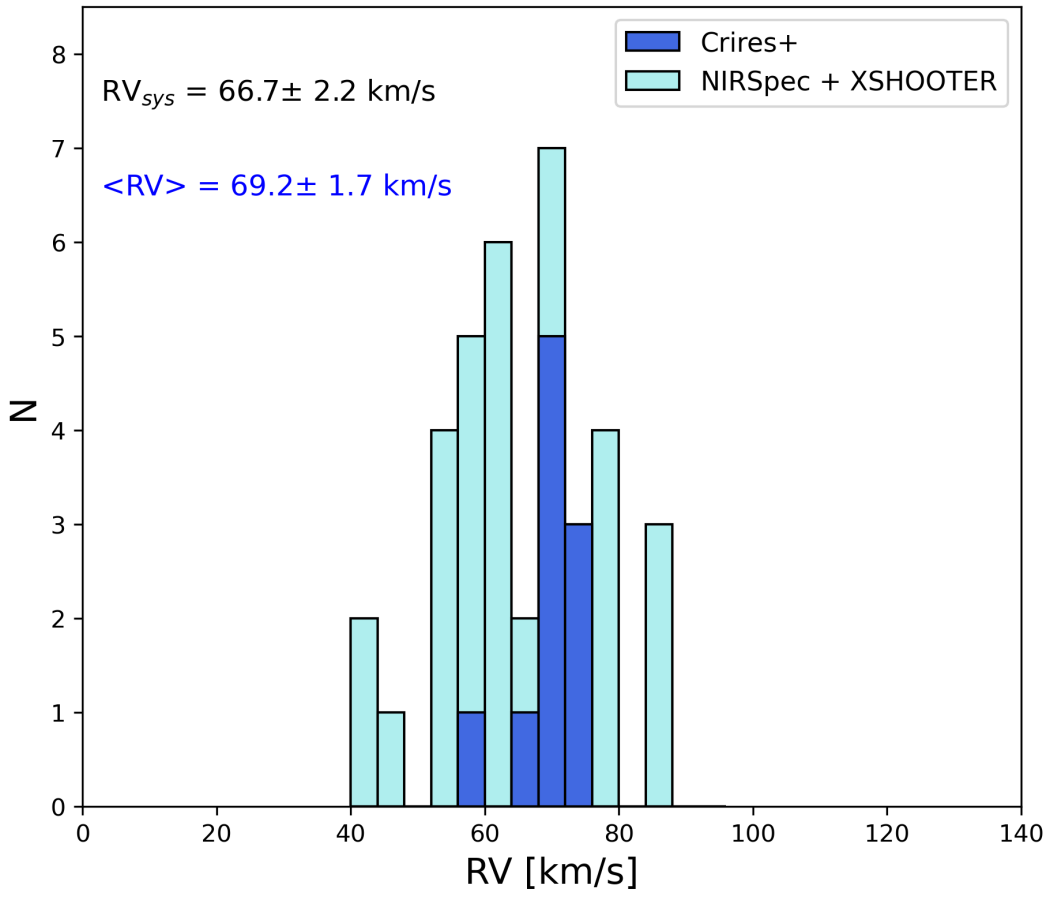

Figure 4.1: *Distribution of radial velocities as measured in this study from Crires+ data (blue histogram), superimposed to the RV distribution of the combined NIRSPec (from Fanelli et al. 2024) and XSHOOTER (from Alvarez Garay et al. 2024) sample (cyan histogram). The systemic radial velocities estimated from the two samples are also reported (in blue and in black for the Crires+ and the NirSpec+XSHOOTER sample, respectively).*

The resulting heliocentric RVs range between 56 and 75 km s^{-1}, with a mean value of 69.2±1.7 km s^{-1} and a 1σ dispersion of 5.2 km s^{-1}. All reported radial velocities have a formal uncertainty smaller than 1 km s^{-1}. The resulting value is in very good agreement with the average RVs quoted in Crociati et al. (2023; 67.9±0.8 km s^{-1}), in Alvarez Garay et al. (2024; 66.6±2.7 km s^{-1}) and in Fanelli et al. (2024; 68.8±3.1 km s^{-1}). The measured RV was found to be in accordance with those observed in previous studies, thereby confirming a systemic RV which is larger than that reported by Baumgardt & Hilker (2018; 60.4±2.4 km s^{-1}).
The radial velocities of all ten stars are within 3σ from the systemic one, thus confirming their membership of Liller 1 according to their 3D kinematics.

4.2 Stellar Parameters

The stellar parameters that have been assumed for each star during the chemical analysis were primarily temperature, gravity, and microturbulence. A reasonable fit to the spectral line core profiles of the analysed stars of Liller 1 is obtained with a microturbulence velocity of 2 km s^{-1}.
With regard to the remaining two parameters, effective temperatures T_{eff} have been determined photometrically within the range 3950–4300 K, with an uncertainty of ±100 K. Similarly, gravities log(g) have been derived within the range 1.25–2.00 dex, with an uncertainty of ±0.3 dex. These values have been obtained by projecting each studied star on a suitable isochrone that reasonably fits the observed CMD. The details of this process are provided in Section 3.4. Global errors (predominantly systematic) on the inferred chemical abundances, obtained by combining the quote source of uncertainties, turn out to be typically in the range 0.1-0.2 dex.
The photometric temperatures have been verified spectroscopically by confirming the absence of any notable trend between the inferred iron abundances and the excitation potential (χ) of the used lines.
As illustrated in Figure 4.2, the iron abundances derived from the various lines exhibit a random distribution around the median value, with no discernible trend associated with the line excitation potential.

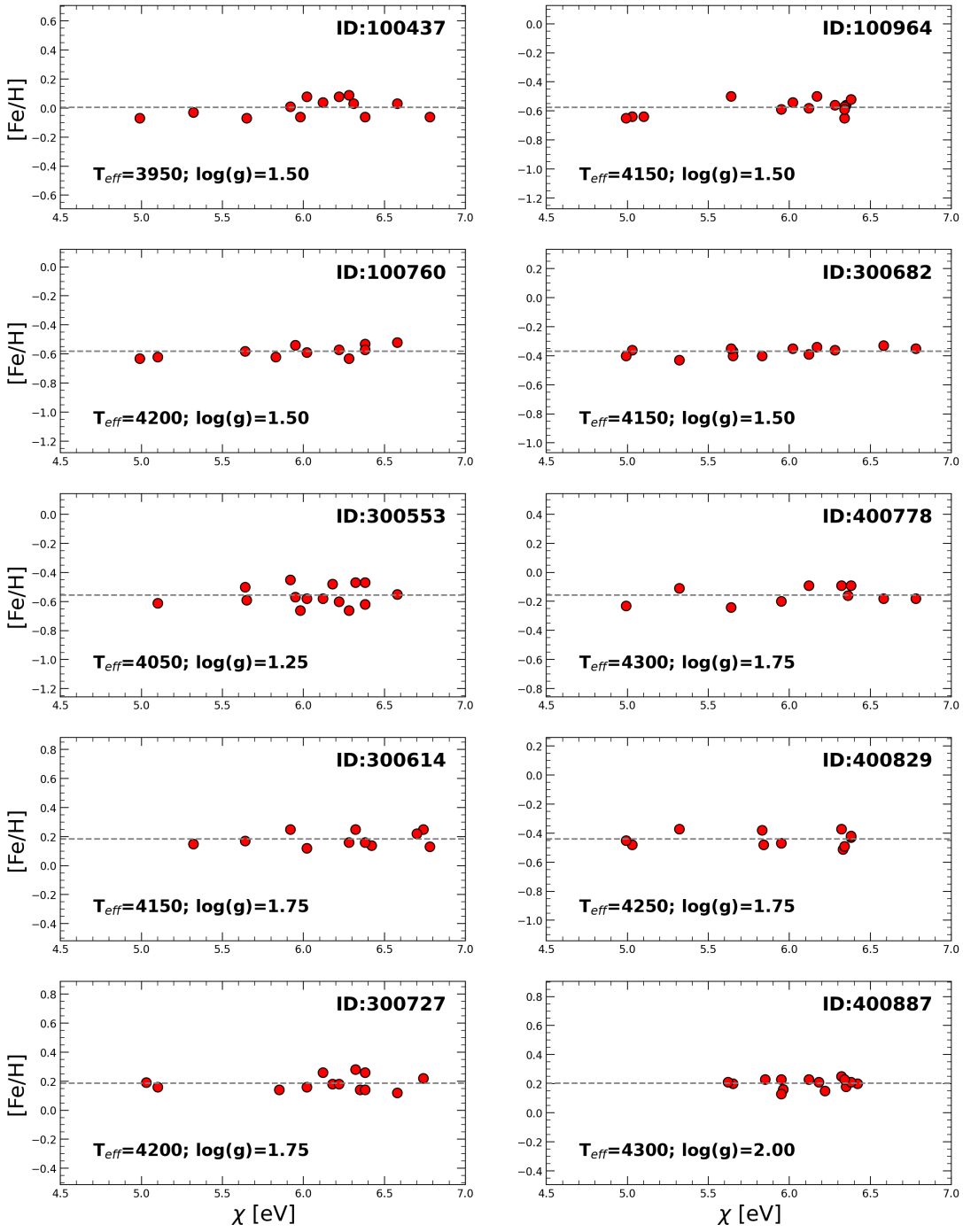

Figure 4.2: *Iron abundances derived from Fe I lines as a function of their excitation potential for the analysed stars. The dashed lines indicate the computed median iron abundances. The lower left of each panel shows the temperature and gravity values of each star in the sample.*

4.3 Chemical abundances

The average chemical abundances of Fe, Mg, Si, S, Ca, Ti, Sc and V for all 10 observed stars of Liller 1, determined via spectral synthesis of the atomic lines (Section

3.4), are reported in Table 4.1.

The corresponding errors for elements with more than one measurable line are typically less than 0.1 dex for each abundance ratio (see Table 4.1). These are statistical errors calculated by dividing the standard deviation by the square root of the number of lines used. In the case of elements with a single measurable line, a conservative 0.1 dex error has been assumed. The occurrence of random errors in the derived abundances is predominantly attributable to the inherent uncertainty associated with the positioning of the continuum (which typically amounts to 1-2%) and to the photon noise present within the spectrum.

The spectra discussed here represents the sample with the highest spectral resolution obtained so far in this stellar system. It is worth of underlying that all the main features of the metallicity distribution previously identified within this cluster are confirmed by the present analysis (Crociati et al. 2023; Alvarez Garay et al. 2024; Fanelli et al. 2024). Indeed, the total sample comprises five metal-poor stars ([Fe/H] $\sim$ -0.5), three super-solar stars ([Fe/H] $\sim$ 0.20) and two stars that can be considered as intermediate with respect to the two main sub-populations. In the following these two stars are marked with green symbols in all the figures.

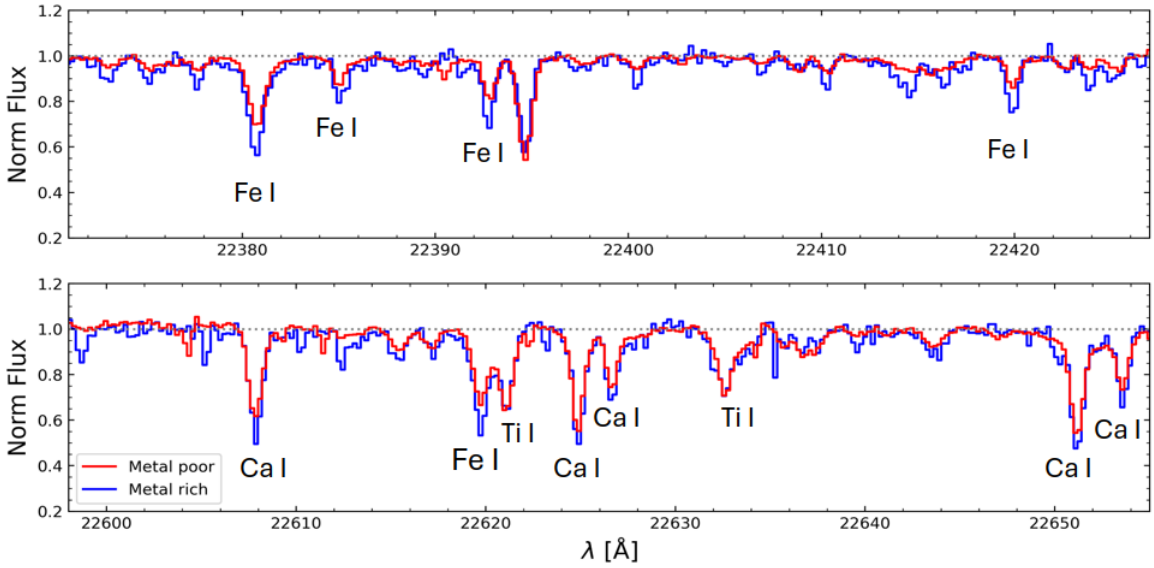

Figure 4.3: *Portions of the K-band spectra of two analysed stars exhibiting different chemical abundances. The metal-poor star (ID300553) is shown in red, while the metal-rich star (ID300727) is illustrated in blue. A select number of atomic lines of interest are also marked.*

Figure 4.3 illustrates portions of the K-band spectrum of two stars with different metallicity. The sub-solar star is plotted in red, while the super-solar star is rep-

resented in blue. The figure also marks some relevant Fe, Ca and Ti spectral lines used for chemical analysis. From the comparison it is quite evident the significant difference between the two spectra, particularly in the depth of the iron lines.

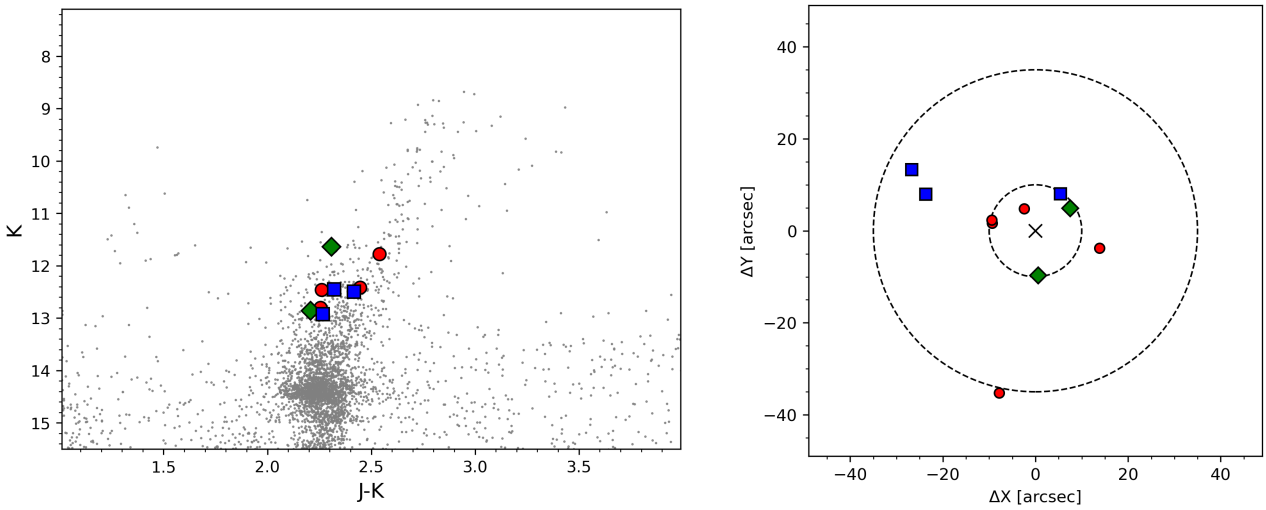

Figure 4.4: *Liller 1 K, J-K CMD (left panel, grey dots) with highlighted the metal-poor (red circles), metal-rich (blue squares) and intermediate (green diamond) likely member stars, for which we measured chemical abundances, and distribution of these stars on the plane of the sky with respect to its center, marked with the black cross and located at* $RA_0 = 263.3523333$, $Dec_0 = -33.3895556$ *(right panel).*

4.3.1 Metallicity

Liller 1 is currently known to host stellar subpopulations with a significant spread in age and metallicity. In particular, it hosts a main stellar component with an old age (12-13 Gyr) and a sub-solar iron abundance, coexisting with additional stellar populations that are super-solar and significantly younger (6-8 Gyr and 1-3 Gyr). Figure 4.5 provides a synthesis of the current understanding of the metallicity distribution in Liller 1. To enhance the statistical power of the analysis, the results of the present study have been integrated with those from Fanelli et al. (2024) and Alvarez Garay et al. (2024), which represent the most recent data available. Fanelli et al. (2024) determined the chemical abundances of 21 giants observed at R $\sim$ 25,000 with NIRSpec, while Alvarez Garay et al. (2024) obtained the abundances of almost the same chemical elements in 27 giants observed at R $\sim$ 8,000 with XSHOOTER. A total of nine stars were in common between the two samples.

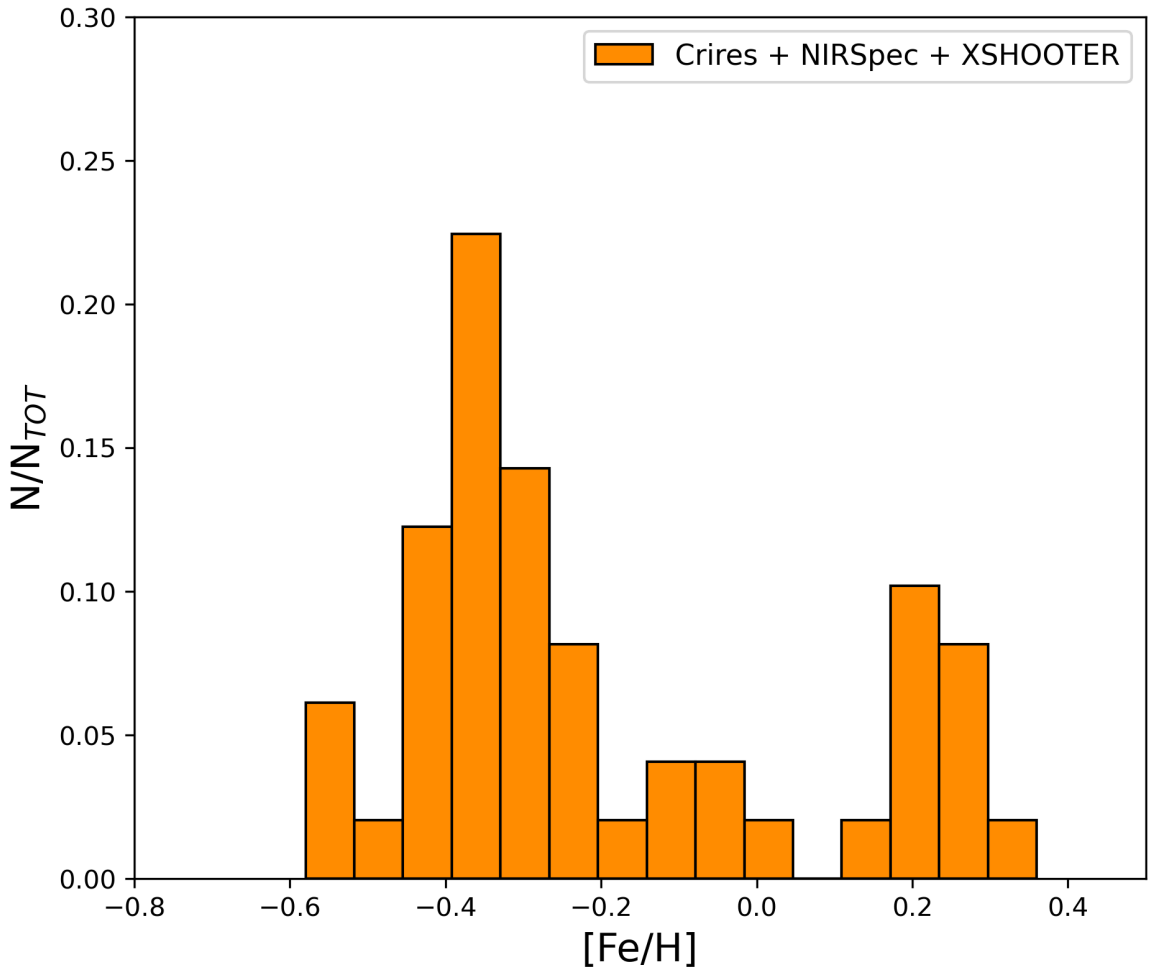

Figure 4.5: *Distribution of the [Fe/H] abundance of Liller1 member stars measured in recent surveys performed with instruments at different resolutions. The results of this work, conducted with CRIRES+ at the VLT, are combined with those obtained from XSHOOTER (Alvarez Garay et al. 2024) and from NIRSpec (Fanelli et al. 2024), in order to facilitate a comprehensive analysis. The total sample comprehends 49 stars, observed at high and intermediate resolution.*

The complete dataset clearly confirms a well defined bimodal distribution, showing a major, sub-solar component counting 37 stars (75%) at an average $[Fe/H] = -0.33 \pm 0.02$ and a super-solar one at an average $[Fe/H] = 0.21 \pm 0.02$, comprising 12 stars (25%).

This result is in accordance with the prediction obtained from the reconstructed star formation history of the system, as determined in the context of a self-enrichment scenario (Dalessandro et al. 2022a), where $\sim 70\%$ of the total mass of the system is expected to form in the first major burst, and the remaining 30% in the following episodes of star formation.

It can thus be confirmed that the existence of multiple stellar components with

different iron abundances, predicted on the basis of the photometric properties of Liller 1 alone, is now corroborated by multi-instrument spectroscopic campaigns.

4.3.2 α-elements

The chemical patterns observed in the [α/Fe]-[Fe/H] diagram permit a more detailed characterisation of these multi-iron sub-populations, and the identification of crucial indications regarding their potential formation scenarios. In fact, as discussed in Chapter 1, the abundance patterns in this diagram are so distinctive that they can be used as "DNA tests" of the stellar population origin.
α-elements (like magnesium, silicon, calcium etc.) are mainly synthesized by massive stars (M>8 $M_{\odot}$) and released to the ISM over a short time scale (10^7 yr) by the explosion of core collapse SNeII. Analysing the formation of the individual elements in more detail:

- Magnesium is a pure α-element. It is only formed by high-mass stars and subsequently ejected by core collapse supernovae.

- Silicon is primarily produced via core-collapse supernovae, through the combustion of oxygen. However, its final abundance is contingent upon a number of factors, as it can be burnt to form calcium.

- Calcium is produced via two distinct formation channels: core-collapse supernovae and thermonuclear supernovae. In the former, which represents the primary site of calcium production, the element is generated through the incomplete combustion of oxygen and silicon.

- Sulfur has a mixed origin because it is produced during the final evolutionary phases of massive stars, but it is also synthesised during SNeII explosions.

- The primary mechanism for the formation of titanium, instead, is the explosion of SNIa. However, it can also be formed through complete and incomplete combustion in the interiors of large-mass stars.

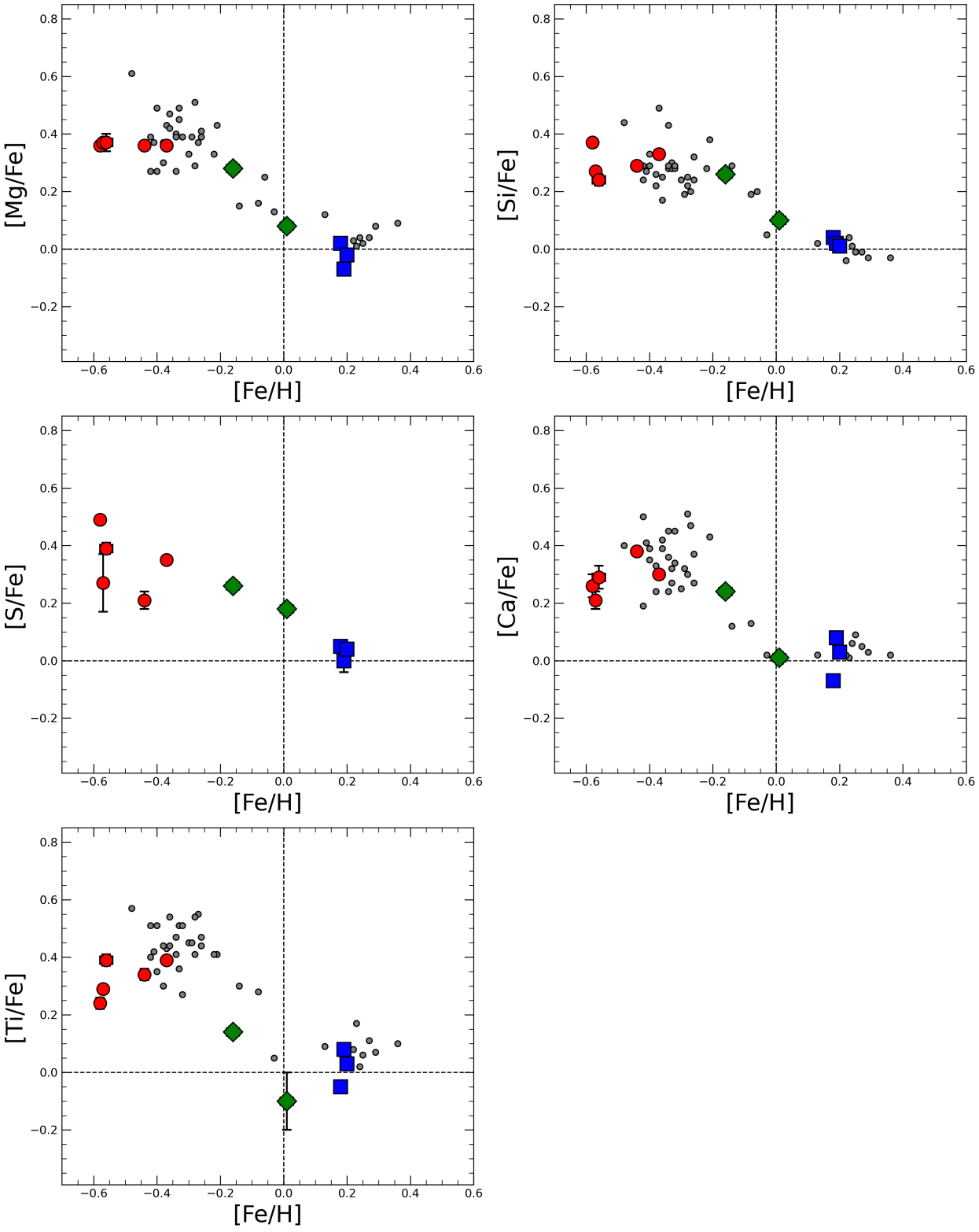

Figure 4.6: *Individual [X/Fe] ratios of Mg, Si, S, Ca, Ti as a function of [Fe/H] for the metal-poor (red circles), metal-rich (blue squares) and intermediate (green diamonds) analysed stars, observed with CRIRES+. Alvarez Garay et al. (2024) and Fanelli et al. (2024) data are reported in the background (grey points).*

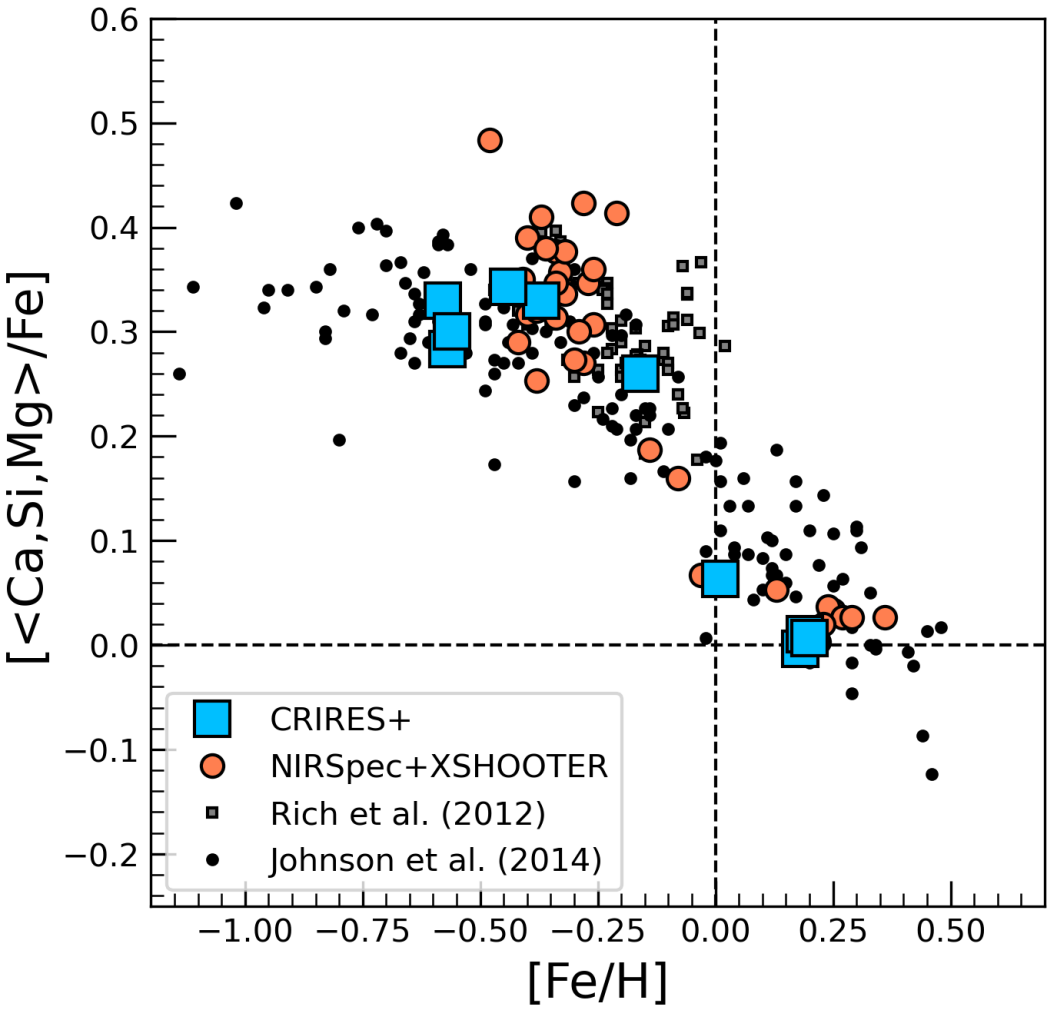

Figure 4.7: *Behaviour of the average α-elements abundance ratio [<Ca,Si,Mg>/Fe] as a function of the metallicity ([Fe/H]) for the 49 stars observed so far in Liller 1 (light blue squares for CRIRES+ stars and smaller orange circles for NIRSpec and XSHOOTER data, already cited in Figure 4.6), compared with the distribution observed for the bulge field stars (grey squares from Rich et al. 2012 and black dots from Johnson et al. 2014).*

Concerning the α-element abundances measured in the CRIRES+ spectra, Fig. 4.6 displays their [X/Fe] abundance ratios as a function of [Fe/H]. A well-defined pattern is observed in all the considered elements. The metal-poor sub-population shows some enhanced (on average by a factor of 2-3) [Mg/Fe], [Si/Fe], [S/Fe], [Ca/Fe] and [Ti/Fe] with respect to the solar value. This finding suggests that this sub-population should have formed rapidly at the early stage of Bulge formation, derived from a gas predominantly enriched by Type II supernova ejecta.

The super-solar component, instead, has about solar-scaled values, with average [X/Fe] between -0.1 and +0.1 dex for most of the measured elements. The absence

of any α-enhancement indicates that this sub-population must have formed from a gas that was enriched also by Type Ia supernova ejecta at at later epoch with respect to the metal-poor one. Interestingly, the stars detected in-between the main metal-poor and metal-rich sub-components, showing intermediate iron content (in the $-0.2 < [Fe/H] < +0.1$ dex range), display also intermediate enhancement in [α/Fe] ratios. The distribution is strikingly similar to that observed in Terzan 5 (Origlia et al. 2011, 2013), and also resembles the bulge field distribution, as can be seen in Fig. 4.7. The dependence of the average abundance of the most representative α-elements (Ca, Si and Mg) on the [Fe/H] abundance of the analysed Liller 1 stars is plotted against the corresponding distribution measured in bulge giant stars from Rich et al. (2012) and from Johnson et al. (2014) for comparison. The two distributions follow exactly the same pattern, therefore unequivocally demonstrating the kinship of Liller 1 with the central region of our galaxy. In fact, as it is well known and explained in Section 1.2, the abundance pattern defined by Galactic bulge stars in the [α/Fe]-[Fe/H] diagram is distinctive within the Local Universe, exhibiting a pronounced knee at metallicity [Fe/H] $\sim$ -0.3 that is markedly higher than the one observed in the MW halo and disk and in dwarf galaxies. This unequivocally demonstrates that the environment where Liller 1 stars formed underwent a particular intense and unique SFR, consequently identifying this pattern as the chemical DNA of the MW bulge.

The growing number of stars exhibiting values of [Fe/H] and [α/Fe] situated between those of the two principal components, as revealed by dedicated spectroscopic screenings, represents a significant indicator that provides crucial insights into the formation scenario of Liller 1. Indeed, the star formation history reconstructed from the analysis of the CMD (Dalessandro et al. 2022a) predicts that Liller 1 has exhibited active star formation throughout its entire lifetime, characterised by three primary episodes: a first, broad episode occurring 12-13 Gyr ago, followed by a prolonged period of low-rate star formation activity, and subsequent intermediate bursts (6-8 Gyr ago) and a very recent burst (2 Gyr ago). It is evident that this would have resulted in the formation of a broad distribution in metallicity and α-elements, which would have retained a record of not only the primary episodes of star formation, but also the collective (low-rate) activity of the stellar system throughout its entire evolutionary history.

4.3.3 Iron-peak elements

The iron-peak elements are defined as those elements with atomic numbers in the range $21 \leq Z \leq 32$, encompassing the elements from scandium to germanium. Scandium (Z = 21) represents a transition between the alpha-elements and the iron-peak elements. These elements are produced in complex nucleosynthesis processes, which allows for their subdivision into two groups. The lower iron group, with atomic numbers between 21 and 26, comprises scandium (Sc), vanadium (V), chromium (Cr), manganese (Mn), and iron (Fe), while the upper iron group includes cobalt (Co), nickel (Ni), copper (Cu), zinc (Zn), gallium (Ga), and germanium (Ge), with atomic numbers between 27 and 32 (Woosley & Weaver 1995; Woosley et al. 2002). Iron-peak elements can be generated by both core-collapse supernovae (including both SNeII and hypernovae) and SNeIa. However, within this group, there are elements that have a preferential formation channel between the two mentioned types of supernova. In general, the lower iron group elements are produced in explosive oxygen burning at temperatures between 3×10^9 and 4×10^9 K, explosive silicon burning at $4 \times 10^9 < T < 5 \times 10^9$ K, or nuclear statistical equilibrium for temperatures exceeding 5×10^9 K (Woosley & Weaver 1995; Nomoto et al. 2013). Instead, the upper iron group elements are produced through neutron capture on iron group nuclei during helium burning and subsequent burning stages, or through the alpha-rich freeze-out from material that has been heated to $T > 5 \times 10^9$ K in the deepest layer. The quantity of each element ejected at the supernova event is contingent upon the mass that falls back.

There is a paucity of analyses of the odd-Z iron-peak elements Sc, V, Mn, Co, and Cu in bulge stars. This may be attributed to the necessity of considering hyperfine structure for these elements and the lack of a substantial number of reliable lines. The present study focuses on the analysis of two iron-peak elements, specifically scandium and vanadium. Their chemical abundance for each star in the sample has been derived from K-band spectra, utilising two distinct scandium lines and a single vanadium line.

Scandium is mainly synthesised within the innermost layers of massive stars and subsequently released into the interstellar medium by core-collapse supernovae. In particular, scandium can be formed either by the burning of neon or by the explosive combustion of oxygen and silicon, as is the case with titanium (Woosley & Weaver 1995; Limongi & Chieffi 2003).

The synthesis of vanadium, instead, can be attributed to two primary sources: the incomplete combustion of silicon in outer layers during the explosive phase of massive stars ($M > 8M_{\odot}$) and Type Ia supernovae. The latter represents a comparatively minor contribution to the former (Woosley & Weaver 1995; Limongi & Chieffi 2003). Figure 4.8 displays the [Sc/Fe] and [V/Fe] abundance ratios as a function of [Fe/H]. Unfortunately, due to the limited number of lines and their possible contamination, scandium abundance was determined for only seven stars in the sample, while vanadium abundance could be obtained for nine stars. All the stars show about solar-scaled [Sc/Fe] and [V/Fe] values with small scatters (-0.10<[Sc/Fe]<+0.20; -0.20<[V/Fe]<0.20). Both [Sc/Fe] and [V/Fe] appear to decrease with increasing metallicity at the high metallicity end, which could be due to enrichment in Fe by supernovae of Type Ia. This is in agreement with previous results found for MW stars (e.g. Howes et al. 2015, 2016; Battistini & Bensby 2015), and confirms the formation of this stellar system within the Milky Way (see Section 1.2 and Fig. 1.4 for reference).

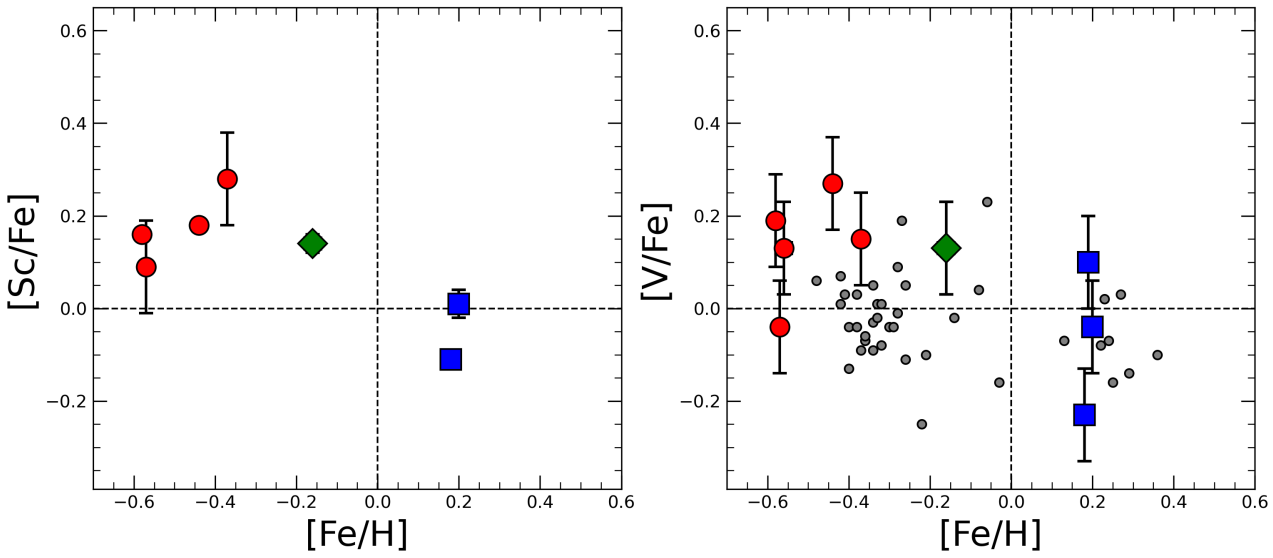

Figure 4.8: Scandium and Vanadium abundance ratios as a function of [Fe/H] for the Liller 1 analysed stars. Sub-solar stars are shown as red circles, while super-solar stars are presented as blue squares. Alvarez Garay et al. (2024) and Fanelli et al. (2024) data are reported in the background (grey points).

4.4 Conclusions and future prospects

This Thesis work presents a high-resolution spectroscopic study in the H and K band of a sample of giant stars (10 objects), members of the Liller 1 bulge stellar system, according to their 3D kinematics. The sample discussed here represents the first portion of a large sample (counting approximately 50 stars) observed in Liller 1 with CRIRES+ that will be analysed in the next months and constitutes the first result of the "Bulge Cluster Origin" (BulCO) survey, which is currently being conducted at the ESO-VLT with the aim of addressing the origin of GCs in the Galactic Bulge. Although the number of stars included in this first portion is limited, they currently are the first sets of spectra at resolution R=50,000 obtained and analysed in this stellar system, thus providing the best view of the available spectral features.
The chemical abundances of Fe, Mg, Si, S, Ca, Ti, Sc and V have been determined and discussed here while the determination of the CNO abundances from CO, OH and CN individual molecular lines is currently undergoing. The derived chemical abundances are discussed in the context of the most recent chemical characterization of the stellar populations hosted in this complex bulge system which is currently based on two sets of data (comprising a total of 39 stars from low/mid-resolution spectroscopy).

The results emerging from this analysis clearly indicate the presence of sub-populations with markedly different iron abundances (spanning approximately 1 dex) and [α/Fe] abundance ratios, exhibiting enhancement at sub-solar metallicities and approximately solar scaling at super-solar metallicities, suggesting that these sub-populations were formed through different star formation events following a self-enrichment scenario. The analysed sample also fully confirmed the existence of the minor, third sub-component (detected also by Fanelli et al. 2024) with [Fe/H] and [α/Fe] abundance ratios somewhat intermediate between the values characterizing the two main sub-populations. This is an important piece of information in reconstructing the origin of Liller 1. In fact, the overall distribution of the Liller 1 stars in the [α/Fe]-[Fe/H] diagram emerging from these studies appears somewhat continuous, thus representing a serious challenge to the scenarios invoking the merging of two globular clusters or the accretion of a giant molecular cloud by a genuine globular cluster, since these events should produce only two distinct sub-populations.

On the other hand, in order to further push our investigation on the Liller 1 origin, I determined the average abundance of the most representative α-elements (Ca, Mg and Si) and compared its dependence on [Fe/H] with the distribution of the same elements drawn by Galactic bulge stars observed at high spectral resolution (by Johnson et al. 2014). The result is plotted in Figure 4.7 and reveals an astonishing similarity: the two distributions follow exactly the same pattern. This clearly testifies an environment that experienced a particularly intense SFR and, because of its uniqueness in the Local Universe, this pattern can be considered as the chemical DNA of the MW bulge. The results shown in Fig. 4.7 therefore unequivocally demonstrates the kinship of Liller 1 with the central region of our galaxy, thus providing compelling support to the hypothesis that this stellar system was born within the MW core and rules out the possibility that the system was accreted from outside the bulge. Furthermore, the determination of scandium and vanadium abundance ratios, which are in agreement with previous abundances found for MW stars, provides additional confirmation of this hypothesis.

The evolutionary, chemical and kinematic information obtained thus far is sufficiently comprehensive to support a scenario where Liller 1 may be the remnant of a much more massive stellar system, as observed in star-forming galaxies at high redshift, that did not fully dissolve to form the bulge, but likely evolved and self-enriched within it as an independent sub-system. It is therefore plausible that the younger sub-populations could be the products of such an evolutionary process. Indeed, due to its large mass, this primordial system would be capable of retaining the SN ejecta and experiencing an almost continuous, low-rate of star formation history, with a few intense bursts, from which iron-enriched stars with different α-enhancement had their origin. A chemical evolution model specifically designed for Liller 1, similar to that discussed in Romano et al. (2023) for Terzan 5, is now under construction (Romano et al. 2024, in preparation). The aim is to provide the detailed properties that the primordial structure should have had in order to originate the observed characteristics of the stellar system. This is essential to characterize the primordial structures that 13 Gyrs ago populated the central region of the Galaxy and that possibly initiated the formation of the Galactic Bulge.

The discovery and characterisation of this intriguing stellar system within the Galactic bulge is further stimulating the search for other candidates of bulge fossil fragments and also the debate about the formation of bulges/spheroids. In this respect, the BulCO survey is performing a high resolution screening of more than 400 giants in 16 additional GCs in the bulge. The same chemical analysis described in this Thesis work will be performed in the next year to the total sample, allowing an unprecedented chemical screening of the GC system of the Galactic Bulge. This will provide the necessary tool to identify the stellar nucleosynthesis and the main chemical enrichment processes of the environment where these ancient and metal-rich stellar systems formed, thus assessing their true origin.

Bibliography

Afşar M., et al., 2018, The Astrophysical Journal, 865, 44

Alvarez R., Plez B., 1998, Near-infrared narrow-band photometry of M-giant and Mira stars: models meet observations (arXiv:astro-ph/9710157), https://arxiv.org/abs/astro-ph/9710157

Alvarez Garay D. A., et al., 2024, Astronomy & Astrophysics, 686, A198

Ballero S. K., Matteucci F., Origlia L., Rich R. M., 2007, Astronomy & Astrophysics, 467, 123

Bastian N., Pfeffer J., 2022, Monthly Notices of the Royal Astronomical Society, 509, 614

Battistini C., Bensby T., 2015, Astronomy & Astrophysics, 577, A9

Baumgardt H., Hilker M., 2018, Monthly Notices of the Royal Astronomical Society, 478, 1520

Baumgardt H., Kroupa P., Parmentier G., 2008, Monthly Notices of the Royal Astronomical Society, 384, 1231

Baumgardt H., Hilker M., Sollima A., Bellini A., 2019, Monthly Notices of the Royal Astronomical Society, 482, 5138

Bournaud F., 2016, in Laurikainen E., Peletier R., Gadotti D., eds, Astrophysics and Space Science Library Vol. 418, Galactic Bulges. p. 355 (arXiv:1503.07660), doi:10.1007/978-3-319-19378-6_13

Bournaud F., Elmegreen B. G., 2009, The Astrophysical Journal Letters, 694, L158

Bournaud F., Elmegreen B. G., Elmegreen D. M., 2007, The Astrophysical Journal, 670, 237–248

Bressan A., Marigo P., Girardi L., Salasnich B., Dal Cero C., Rubele S., Nanni A., 2012, Monthly Notices of the Royal Astronomical Society, 427, 127

Cadelano M., et al., 2023, Astronomy & Astrophysics, 679, L13

Carretta E., Bragaglia A., 2023, Astronomy & Astrophysics, 677, A73

Carretta E., et al., 2009, Astronomy & Astrophysics, 505, 117

Carretta E., Bragaglia A., Gratton R. G., Recio-Blanco A., Lucatello S., D'Orazi V., Cassisi S., 2010, Astronomy & Astrophysics, 516, A55

Chiappini C., Matteucci F., Beers T. C., Nomoto K., 1999, The Astrophysical Journal, 515, 226

Crociati C., et al., 2023, The Astrophysical Journal, 951, 17

D'Ercole A., Vesperini E., D'Antona F., McMillan S. L. W., Recchi S., 2008, Monthly Notices of the Royal Astronomical Society, 391, 825

Dalessandro E., et al., 2016, The Astrophysical Journal, 833, 111

Dalessandro E., et al., 2022a, The Astrophysical Journal, 940, 170

Dalessandro E., et al., 2022b, The Astrophysical Journal, 940, 170

Davis M., Efstathiou G., Frenk C. S., White S. D. M., 1985, The Astrophysical Journal, 292, 371

Deras D., Cadelano M., Ferraro F. R., Lanzoni B., Pallanca C., 2023, The Astrophysical Journal, 942, 104

Elmegreen B. G., Bournaud F., Elmegreen D. M., 2008, The Astrophysical Journal, 688, 67

Elmegreen B. G., Elmegreen D. M., Fernandez M. X., Lemonias J. J., 2009, The Astrophysical Journal, 692, 12

Fanelli C., Origlia L., Oliva E., Mucciarelli A., Sanna N., Dalessandro E., Romano D., 2021, Astronomy & Astrophysics, 645, A19

Fanelli C., Origlia L., Oliva E., Dalessandro E., Mucciarelli A., Sanna N., 2022, Astronomy & Astrophysics, 660, A7

Fanelli C., et al., 2024, arXiv e-prints, p. arXiv:2408.12649

Ferraro F. R., Montegriffo P., Origlia L., Fusi Pecci F., 2000, The Astronomical Journal, 119, 1282

Ferraro F. R., et al., 2009, Nature, 462, 483

Ferraro F. R., Massari D., Dalessandro E., Lanzoni B., Origlia L., Rich R. M., Mucciarelli A., 2016, The Astrophysical Journal, 828, 75

Ferraro F. R., et al., 2018, The Astrophysical Journal, 860, 50

Ferraro F. R., et al., 2021a, Nature Astronomy, 5, 311

Ferraro F. R., et al., 2021b, Nature Astronomy, 5, 311–318

Gaia Collaboration et al., 2016, Astronomy & Astrophysics, 595, A1

Gaia Collaboration et al., 2023, Astronomy & Astrophysics, 674, A1

Geisler D., Smith V. V., Wallerstein G., Gonzalez G., Charbonnel C., 2005, The Astronomical Journal, 129, 1428

Genzel R., et al., 2011, The Astrophysical Journal, 733, 101

Grieco V., Matteucci F., Pipino A., Cescutti G., 2012, Astronomy & Astrophysics, 548, A60

Gustafsson B., Edvardsson B., Eriksson K., Jørgensen U. G., Nordlund Å., Plez B., 2008, Astronomy & Astrophysics, 486, 951

Harris W. E., 1996, The Astronomical Journal, 112, 1487

Harris W. E., 2010, arXiv e-prints, p. arXiv:1012.3224

Helmi A., 2020, Annual Review of Astronomy and Astrophysics, 58, 205

Howes L. M., et al., 2015, Nature, 527, 484

Howes L. M., et al., 2016, Monthly Notices of the Royal Astronomical Society, 460, 884

Immeli A., Samland M., Gerhard O., Westera P., 2004, Astronomy & Astrophysics, 413, 547

Jeřábková T., Hasani Zonoozi A., Kroupa P., Beccari G., Yan Z., Vazdekis A., Zhang Z. Y., 2018, Astronomy & Astrophysics, 620, A39

Johnson C. I., Rich R. M., Kobayashi C., Kunder A., Koch A., 2014, The Astronomical Journal, 148, 67

Khoperskov S., Mastrobuono-Battisti A., Di Matteo P., Haywood M., 2018, Astronomy & Astrophysics, 620, A154

Kobayashi C., Karakas A. I., Lugaro M., 2020, The Astrophysical Journal, 900, 179

Koch A., Grebel E. K., Gilmore G. F., Wyse R. F. G., Kleyna J. T., Harbeck D. R., Wilkinson M. I., Evans N. W., 2008, The Astronomical Journal, 135, 1580

Lanzoni B., Dalessandro E., Ferraro F. R., Miocchi P., Valenti E., Rood R. T., 2007, The Astrophysical Journal Letters, 668, L139

Lanzoni B., et al., 2010, The Astrophysical Journal, 717, 653

Lanzoni B., et al., 2013, The Astrophysical Journal, 769, 107

Lemasle B., et al., 2012, Astronomy & Astrophysics, 538, A100

Letarte B., 2007, PhD thesis, University of Groningen, Netherlands

Libralato M., et al., 2022, The Astrophysical Journal, 934, 150

Lim D., Koch-Hansen A. J., Chun S.-H., Hong S., Lee Y.-W., 2022, Astronomy & Astrophysics, 666, A62

Limongi M., Chieffi A., 2003, The Astrophysical Journal, 592, 404

Lockwood A. C., Johnson J. A., Bender C. F., Carr J. S., Barman T., Richert A. J. W., Blake G. A., 2014, The Astrophysical Journal, 783, L29

Lomaeva M., Jönsson H., Ryde N., Schultheis M., Thorsbro B., 2019, Astronomy & Astrophysics, 625, A141

Marino A. F., Milone A. P., Piotto G., Villanova S., Bedin L. R., Bellini A., Renzini A., 2009, Astronomy & Astrophysics, 505, 1099

Massari D., et al., 2012, The Astrophysical Journal Letters, 755, L32

Massari D., et al., 2014, The Astrophysical Journal, 795, 22

Massari D., et al., 2015, The Astrophysical Journal, 810, 69

Massari D., Koppelman H. H., Helmi A., 2019, Astronomy & Astrophysics, 630, L4

Mastrobuono-Battisti A., Khoperskov S., Di Matteo P., Haywood M., 2019, Astronomy & Astrophysics, 622, A86

Matteucci F., Brocato E., 1990, The Astrophysical Journal, 365, 539

Matteucci F., Chiappini C., 2005, Publications of the Astronomical Society of Australia, 22, 49

McKenzie M., Bekki K., 2018, Monthly Notices of the Royal Astronomical Society, 479, 3126

McWilliam A., Smecker-Hane T. A., 2005, in Barnes Thomas G. I., Bash F. N., eds, Astronomical Society of the Pacific Conference Series Vol. 336, Cosmic Abundances as Records of Stellar Evolution and Nucleosynthesis. p. 221 (arXiv:astro-ph/0409083), doi:10.48550/arXiv.astro-ph/0409083

McWilliam A., Matteucci F., Ballero S., Rich R. M., Fulbright J. P., Cescutti G., 2008, The Astronomical Journal, 136, 367

Milone A. P., et al., 2017, Monthly Notices of the Royal Astronomical Society, 464, 3636

Minelli A., Mucciarelli A., Romano D., Bellazzini M., Origlia L., Ferraro F. R., 2021a, The Astrophysical Journal, 910, 114

Minelli A., Mucciarelli A., Massari D., Bellazzini M., Romano D., Ferraro F. R., 2021b, The Astrophysical Journal Letters, 918, L32

Monaco L., Bellazzini M., Bonifacio P., Ferraro F. R., Marconi G., Pancino E., Sbordone L., Zaggia S., 2005, Astronomy & Astrophysics, 441, 141

Mucciarelli A., Lapenna E., Massari D., Pancino E., Stetson P. B., Ferraro F. R., Lanzoni B., Lardo C., 2015, The Astrophysical Journal, 809, 128

Mucciarelli A., Massari D., Minelli A., Romano D., Bellazzini M., Ferraro F. R., Matteucci F., Origlia L., 2021, Nature Astronomy, 5, 1247

Ness M., et al., 2013, Monthly Notices of the Royal Astronomical Society, 430, 836

Nomoto K., Kobayashi C., Tominaga N., 2013, Annual Review of Astronomy and Astrophysics, 51, 457

Origlia L., Rich R. M., 2004, The Astronomical Journal, 127, 3422

Origlia L., Ferraro F. R., Fusi Pecci F., Oliva E., 1997, Astronomy and Astrophysics, 321, 859

Origlia L., Rich R. M., Castro S., 2002, The Astronomical Journal, 123, 1559

Origlia L., Ferraro F. R., Bellazzini M., Pancino E., 2003, The Astrophysical Journal, 591, 916

Origlia L., Valenti E., Rich R. M., 2005, Monthly Notices of the Royal Astronomical Society, 356, 1276

Origlia L., Valenti E., Rich R. M., 2008, Monthly Notices of the Royal Astronomical Society, 388, 1419

Origlia L., et al., 2011, The Astrophysical Journal Letters, 726, L20

Origlia L., Massari D., Rich R. M., Mucciarelli A., Ferraro F. R., Dalessandro E., Lanzoni B., 2013, The Astrophysical Journal Letters, 779, L5

Pallanca C., et al., 2021, The Astrophysical Journal, 917, 92

Pallanca C., et al., 2023, The Astrophysical Journal, 950, 138

Pfeffer J., Lardo C., Bastian N., Saracino S., Kamann S., 2021, Monthly Notices of the Royal Astronomical Society, 500, 2514

Plez B., 2012, Turbospectrum: Code for spectral synthesis, Astrophysics Source Code Library, record ascl:1205.004

Rich R. M., Origlia L., Valenti E., 2012, The Astrophysical Journal, 746, 59

Romano D., Karakas A. I., Tosi M., Matteucci F., 2010, Astronomy & Astrophysics, 522, A32

Romano D., et al., 2023, The Astrophysical Journal, 951, 85

Ryabchikova T., Pakhomov Y., 2015, Baltic Astronomy, 24, 453

Saracino S., et al., 2015, The Astrophysical Journal, 806, 152

Saracino S., et al., 2016, The Astrophysical Journal, 832, 48

Saracino S., et al., 2019, The Astrophysical Journal, 874, 86

Sbordone L., Bonifacio P., Buonanno R., Marconi G., Monaco L., Zaggia S., 2007, Astronomy & Astrophysics, 465, 815

Shetrone M., Venn K. A., Tolstoy E., Primas F., Hill V., Kaufer A., 2003, The Astronomical Journal, 125, 684

Skúladóttir Á., Tolstoy E., Salvadori S., Hill V., Pettini M., 2017, Astronomy & Astrophysics, 606, A71

Tacchella S., et al., 2015, The Astrophysical Journal, 802, 101

Tam P. H. T., Kong A. K. H., Hui C. Y., Cheng K. S., Li C., Lu T. N., 2011, The Astrophysical Journal, 729, 90

Tolstoy E., Hill V., Tosi M., 2009, Annual Review of Astronomy and Astrophysics, 47, 371

Tsujimoto T., Bekki K., 2012, The Astrophysical Journal, 747, 125

Valenti E., Origlia L., Ferraro F. R., 2005, Monthly Notices of the Royal Astronomical Society, 361, 272

Valenti E., Ferraro F. R., Origlia L., 2007, The Astronomical Journal, 133, 1287

Valenti E., Ferraro F. R., Origlia L., 2010, Monthly Notices of the Royal Astronomical Society, 402, 1729–1739

Valenti E., et al., 2016, Astronomy & Astrophysics, 587, L6

Venn K. A., Irwin M., Shetrone M. D., Tout C. A., Hill V., Tolstoy E., 2004, The Astronomical Journal, 128, 1177

Verbunt F., Hut P., 1987, in Helfand D. J., Huang J. H., eds, IAU Symposium Vol. 125, The Origin and Evolution of Neutron Stars. p. 187

Weiland J. L., et al., 1994, The Astrophysical Journal Letters, 425, L81

Woosley S. E., Weaver T. A., 1995, Astrophysical Journal Supplement, 101, 181

Woosley S. E., Heger A., Weaver T. A., 2002, Reviews of Modern Physics, 74, 1015

Yan Z., Jerabkova T., Kroupa P., 2017, Astronomy & Astrophysics, 607, A126

de Laverny P., Recio-Blanco A., Worley C. C., Plez B., 2012, Astronomy & Astrophysics, 544, A126